Ocean Engineering 357 (2026) 125524

Contents lists available at ScienceDirect

Ocean Engineering

journal homepage: www.elsevier.com/locate/oceaneng

Research paper

CFD analysis of wind-wave misalignment effects on the aero-hydrodynamic performance and wake characteristic of the floating offshore wind turbine

Yingjie Xue [a], Jinguang Wang [b], Weiwen Zhao [a,*], Decheng Wan [a]

[a] Computational Marine Hydrodynamic Lab (CMHL), School of Ocean and Civil Engineering, Shanghai Jiao Tong University, Shanghai, 200240, China
[b] Zhongnan Engineering Corporation Limited, Changsha, 410027, China

ARTICLE INFO

Keywords:
Floating offshore wind turbine
Computational fluid dynamics
Wind-wave misalignment
Oblique waves
Aero-hydrodynamic response

ABSTRACT

Present study employs computational fluid dynamics simulations to investigate the aero-hydrodynamic behavior of an OC4 semi-submersible floating offshore wind turbine under wind-wave misalignment conditions. The OpenFOAM-based toolbox waves2Foam is extended to generate shear wind and coupled with the in-house solver fully coupled aero-hydro-elastic-servo solver FOWT-UALM-SJTU. It has been rigorously validated through steady and unsteady aerodynamic predictions, hydrodynamic response under wave-only conditions, and fully coupled simulations, demonstrating good agreement with experimental and numerical data. Simulations across five wave (misalignment) directions (0°, 15°, 30°, 45°, 60°) reveal that oblique waves reduce surge and pitch amplitudes while exciting significant sway and roll oscillations. At 60° wave direction, mooring tensions in lines #1 and #2 become comparable. Aerodynamically, rotor power remains stable while thrust exhibits minimal fluctuation at 30° when accounting for gravitational effects. Flow analysis demonstrates that oblique conditions enhance wake meandering and vortex fragmentation, improving wake recovery and available power. This research establishes a simulation framework for misaligned wind-wave conditions, providing valuable data for the design of floating wind turbines in real sea environments.

1. Introduction

With growing emphasis on clean energy, the wind energy industry has developed rapidly. In recent years, offshore wind energy has attracted significant attention due to its extensive wind resources, lower turbulence intensity, and remote location from urban areas (Esteban et al., 2011; Xu et al., 2022). According to the Global Wind Energy Council (GWEC, 2025), by 2024, total offshore wind installations had reached 83.2 GW (gigawatt). Over the past five years (2020–2024), new offshore installations amounted to 54 GW, accounting for 64.90% of cumulative offshore capacity. Predictions suggest the global new offshore installations will reach 34 GW by 2030. As a representative type of deep-water wind energy technology, floating offshore wind turbines (FOWTs) are predominantly utilized at depths beyond 60 m (Bagbanci et al., 2012). Their complex operational environment imposes stricter requirements on design, installation, operation, and maintenance, motivating extensive research on FOWTs (Micallef and Rezaeiha, 2021; Ramachandran et al., 2022).

Aerodynamic and hydrodynamic analysis of FOWTs primarily employs two approaches: physical model tests and numerical simulations are two primary approaches. While wind tunnel and marine tank tests offer valuable empirical foundations, they face fundamental limitations. It remains challenging to simultaneously satisfy both Reynolds number similarity (critical for aerodynamics) and Froude number similarity (essential for hydrodynamics) (Chen et al., 2020; Otter et al., 2022). Scaling effects, coupled aero-hydrodynamic complexities, and inadequate wake representation (Chen et al., 2025) further limit the accuracy of integrated model testing for engineering design. In contrast, numerical simulations offer a more flexible framework, typically categorized into mid-fidelity tools and high-fidelity Computational Fluid Dynamics (CFD). In this study, we employ the mid-fidelity tool OpenFAST (NREL, 2025) to provide validation data, while high-fidelity, fully coupled aero-hydrodynamic simulations are performed using the in-house CFD solver FOWT-UALM-SJTU (Li et al., 2015; Cheng et al., 2019; Huang et al., 2024), based on OpenFOAM.

OpenFAST, initially developed by the National Renewable Energy Laboratory (NREL) as FAST (Jonkman and Buhl, 2025), is the predominant open-source simulation suite in FOWT research. It features a modular architecture that integrates AeroDyn for aerodynamics, HydroDyn for hydrodynamics, MoorDyn for mooring dynamics, and

* Corresponding author.
E-mail address: weiwen.zhao@sjtu.edu.cn (W. Zhao).

https://doi.org/10.1016/j.oceaneng.2026.125524
Received 12 November 2025; Received in revised form 1 April 2026; Accepted 8 April 2026
Available online 21 April 2026

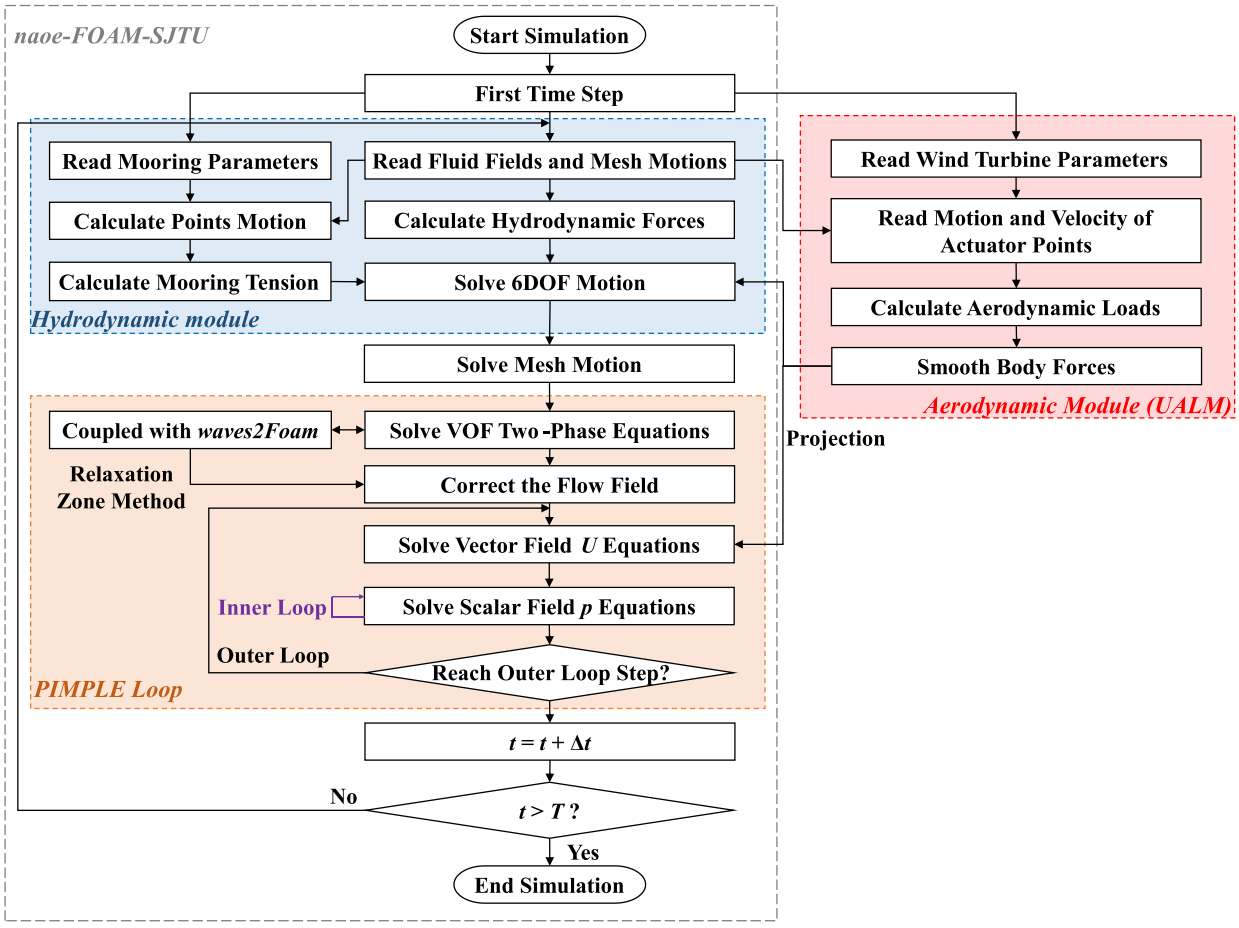

Fig. 1. Framework of FOWT-UALM-SJTU solver (Xue et al., 2025).

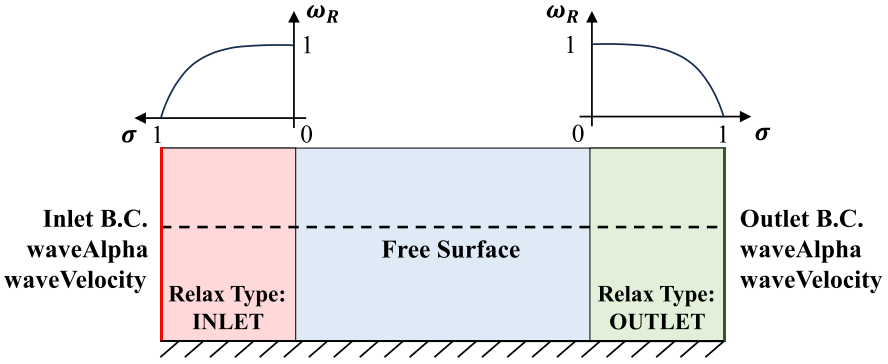

Fig. 2. Relaxation type settings and the relationship between ω_R and σ.

BeamDyn for aeroelasticity within the OpenFAST and FAST.Farm solver. The framework employs multi-fidelity aerodynamic models, including the Blade Element Momentum (BEM), Generalized Dynamic Wake (GDW) and Free Vortex Wake (FVW) methods, and supports integration with high-fidelity wind fields from OpenFOAM (Shaler et al., 2019) and ExaWind (Ananthan et al., 2019; Branlard et al., 2024). The academic community has further enhanced OpenFAST's capabilities through various extensions. Notable examples include couplings with Nemoh (Kurnia and Ducrozet, 2023), HAMS (Liu, 2019), OrcaFlex (Deng et al., 2025), TIMEFLOAT (Roddier et al., 2010), CHARM3D (Shim, 2009), AQWA (by F2A) (Yang et al., 2020), and the Finite Element Method (FEM)-based solver SeaFEM (Berdugo-Parada et al., 2024). These developments, combined with the software's open-source nature and robust validation history, have established OpenFAST as the standard in academic FOWT research. Therefore, this study employs it for partial numerical validation of our CFD framework, leveraging its well-documented reliability.

High-fidelity CFD techniques, which solve the Navier-Stokes equations, are capable of accurately simulating viscous flow effects, wave impacts, and wake dynamics (Zhang et al., 2024). OpenFOAM, as a leading open-source CFD tool, is widely adopted in academia due to its open architecture, which facilitates the integration of custom numerical methods and modules, like the wave generation toolbox waves2Foam (Jacobsen, 2017) and MoorDyn-coupling tool (Chen and Hall, 2022). Within FOWT research, OpenFOAM has been extensively customized to enable fully coupled simulations. One trajectory employs full resolved

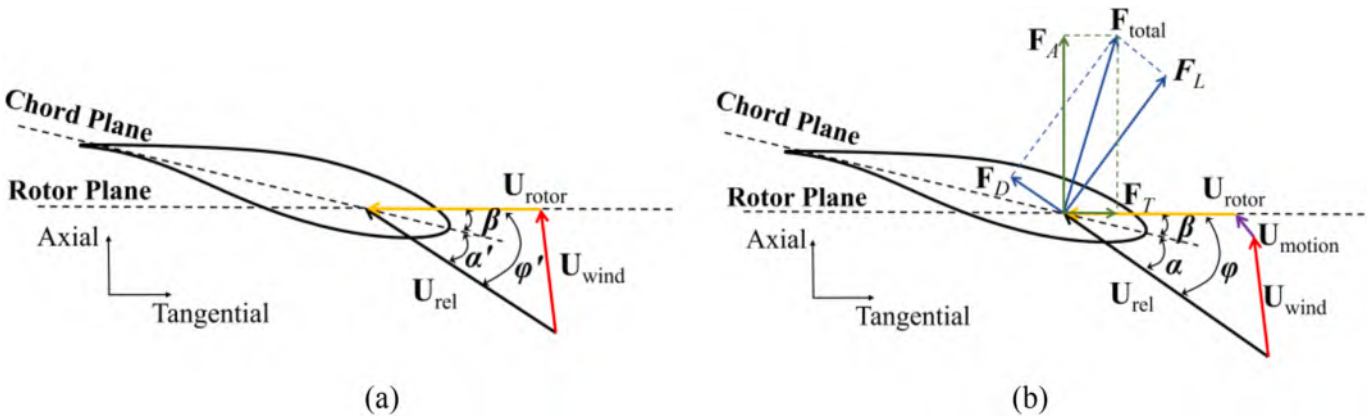

Fig. 3. Cross-sectional airfoil element: (a) traditional ALM airfoil; (b) UALM method airfoil.

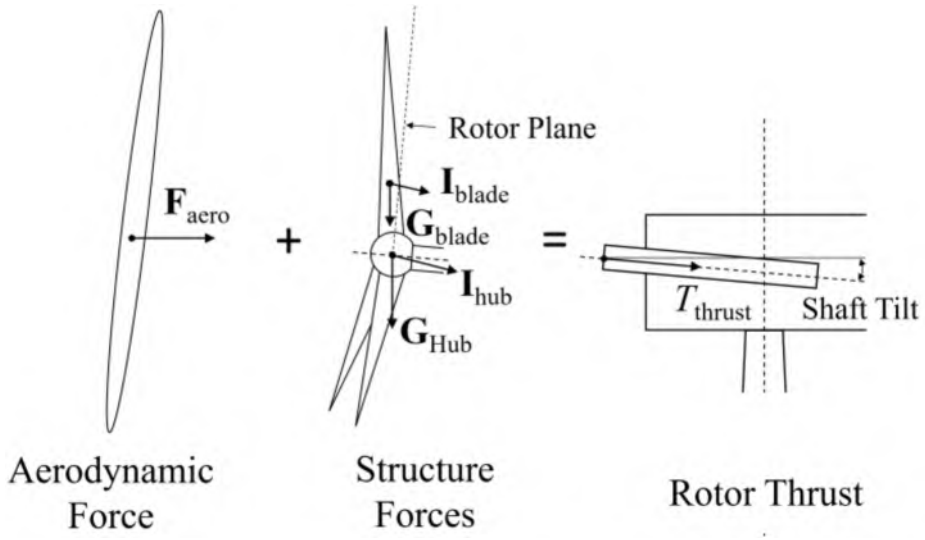

Fig. 4. Force decomposition of rotor thrust.

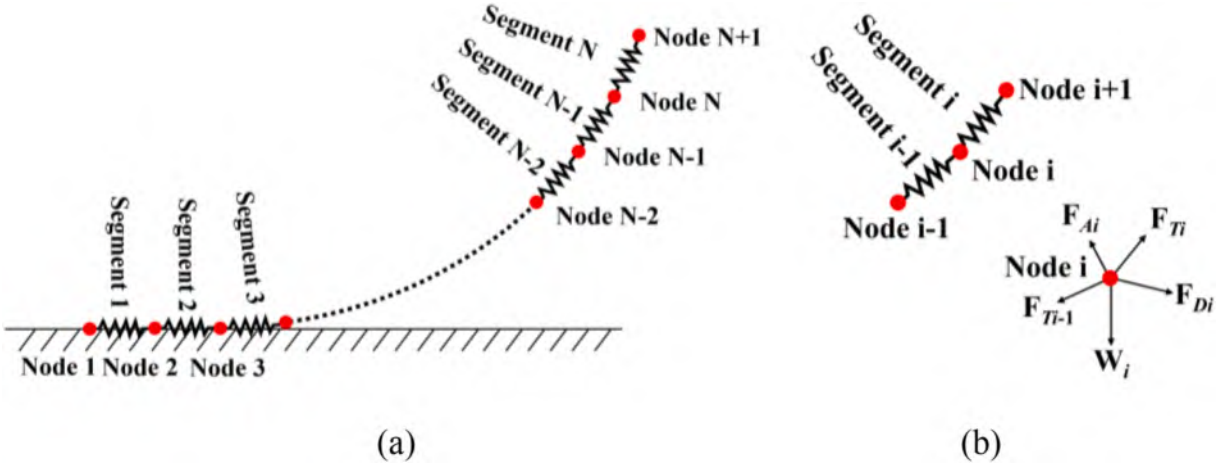

Fig. 5. Sketch of mooring line in LMM: (a) entire mooring line; (b) forces exerted on Node *i*.

structural modeling, as seen in the works of Liu et al. (2017, 2019b), who utilized OpenFOAM's Arbitrary Mesh Interface for FOWT simulation and later integrated MBDyn for aeroelastic blade analysis. Zhou et al. (2019, 2022) extended this framework by incorporating turbulent wind spectra and waves2Foam for complex wind and wave conditions.

The second trajectory focuses on implementing efficient aerodynamic models, primarily through the Actuator Disk (AD) and Actuator Line Model (ALM) methods, such as SOWFA by NREL (Churchfield et al., 2012) and turbinesFoam (Bachant et al., 2016). Pericàs (2022) coupled turbinesFoam with OpenFOAM's rigid body motion module to achieve

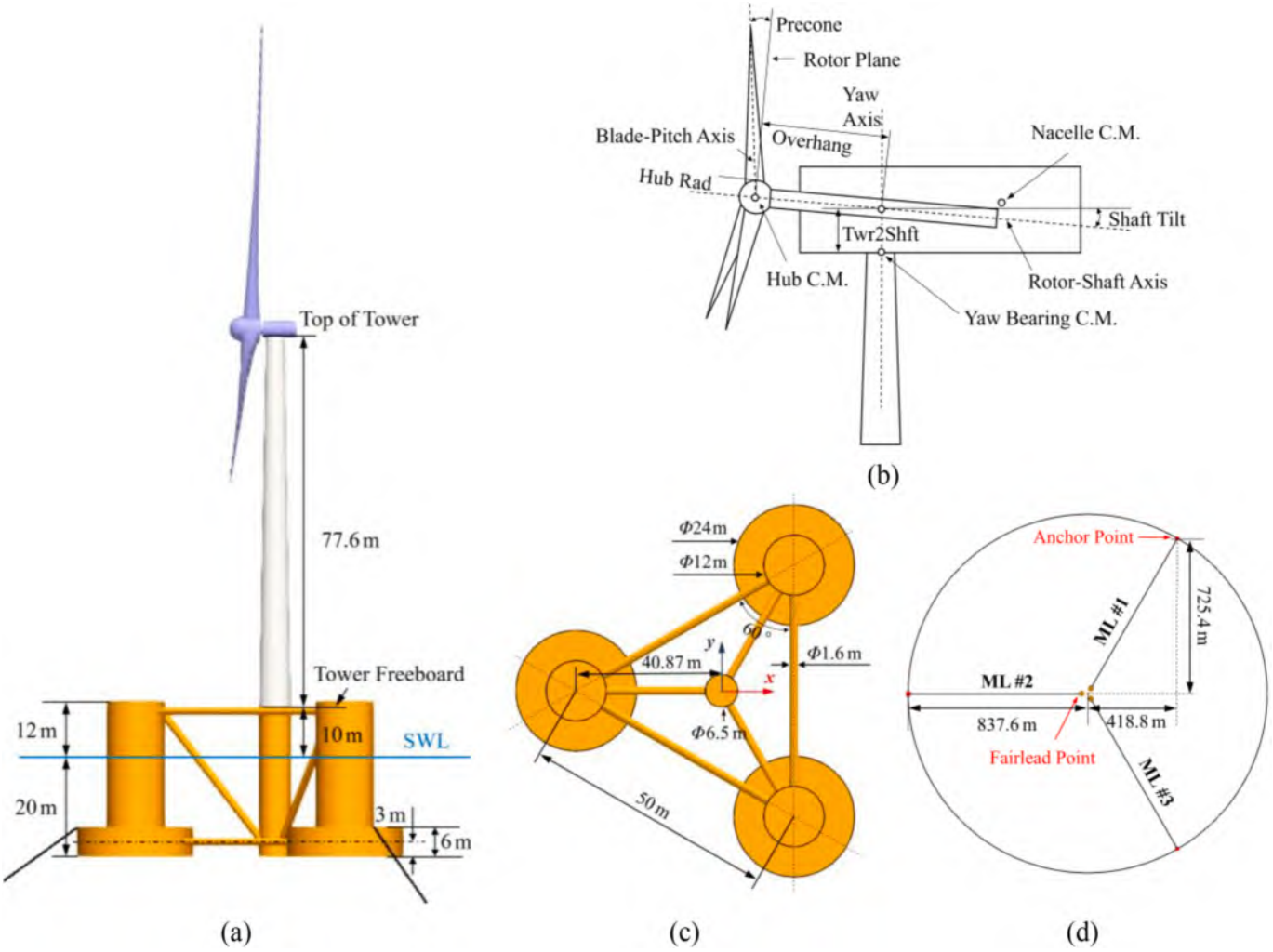

Fig. 6. OC4 FOWT model: (a) overall FOWT model (SWL: Still Water Level); (b) wind turbine; (c) OC4 platform; (d) mooring system.

Table 1
Overall properties of OC4 FOWT used for simulation.

Properties	Value
Entire FOWT mass	14,072,718 kg
FOWT C.M. location bellow SWL	9.889 m
FOWT roll inertia about C.M. (I_{xx})	1.07116×10^{10} kg m^2
FOWT pitch inertia about C.M. (I_{yy})	1.07116×10^{10} kg m^2
FOWT yaw inertia about C.M. (I_{zz})	1.226×10^{10} kg m^2

Unsteady ALM (UALM) considering the platform's motions, and integrated waves2Foam for fully coupled simulations. Cai et al. (2025) extended this framework to a more comprehensive FOWT solver MRFoam, by integrating the MoorDyn-coupling tool. Yu et al. (2023) developed a coupled turbinesFoam-BeamDyn interface, and extended a FEM-based solver qaleFoam (Li et al., 2018) to qaleFoam-BE. Liu et al. (2015), Cheng et al. (2019), and Huang et al. (2024) from our group coupled SOWFA to develop the aero-hydro-elastic-servo solver FOWT-UALM-SJTU, which is used in present study and detailed in Section 2. The third trajectory is hybrid paradigm, which utilizes multi-fidelity tools to further improve computational efficiency. The typical representative is SOWFA, which could employ OpenFOAM for aerodynamics and OpenFAST for hydrodynamics, enabling high-fidelity simulation of FOWT wake fields (Xu et al., 2023). Campaña-Alonso et al. (2023) proposed the OF^2 solver, combining OpenFOAM for hydrodynamics and OpenFAST for aerodynamics. Kim et al. (2025) coupled a higher-order spectral viscous-potential flow coupling solver foamStar (Choi et al., 2020) with OpenFAST to achieve aero-hydro-servo-elastic simulations. In summary, the use of OpenFOAM for CFD has been widely applied in FOWT numerical calculations, and it has significant advantages in dealing with complex coupled problems.

In real ocean environments, oblique waves and wind-wave

Table 2
Simulation conditions.

Cases	Wind speed (m/s)	Stokes 2nd-order wave $H = 7.58$ m, $T = 12.1$s	Rotor speed (rpm)	Platform motion	UALM Projection width factor	Simulation time (s)
LC.1.1–LC.1.3	11.4	×	12.1	Fixed	4.0, 4.2, 4.4	200 (dt = 0.01)
LC.1.4–LC.1.27	3–25, 11.4	×	Control system	Fixed	4.2	200 (dt = 0.01)
LC.2	11	×	12	Forced	4.2	800 (dt = 0.005)
LC.3.1–LC.3.3	0	0°	0	6 DoF	4.2	800 (dt = 0.005)
LC.4.1–LC.4.5	11.4 (shear)	0°, 15°, 30°, 45°, 60°	12.1	6 DoF	4.2	800 (dt = 0.005)

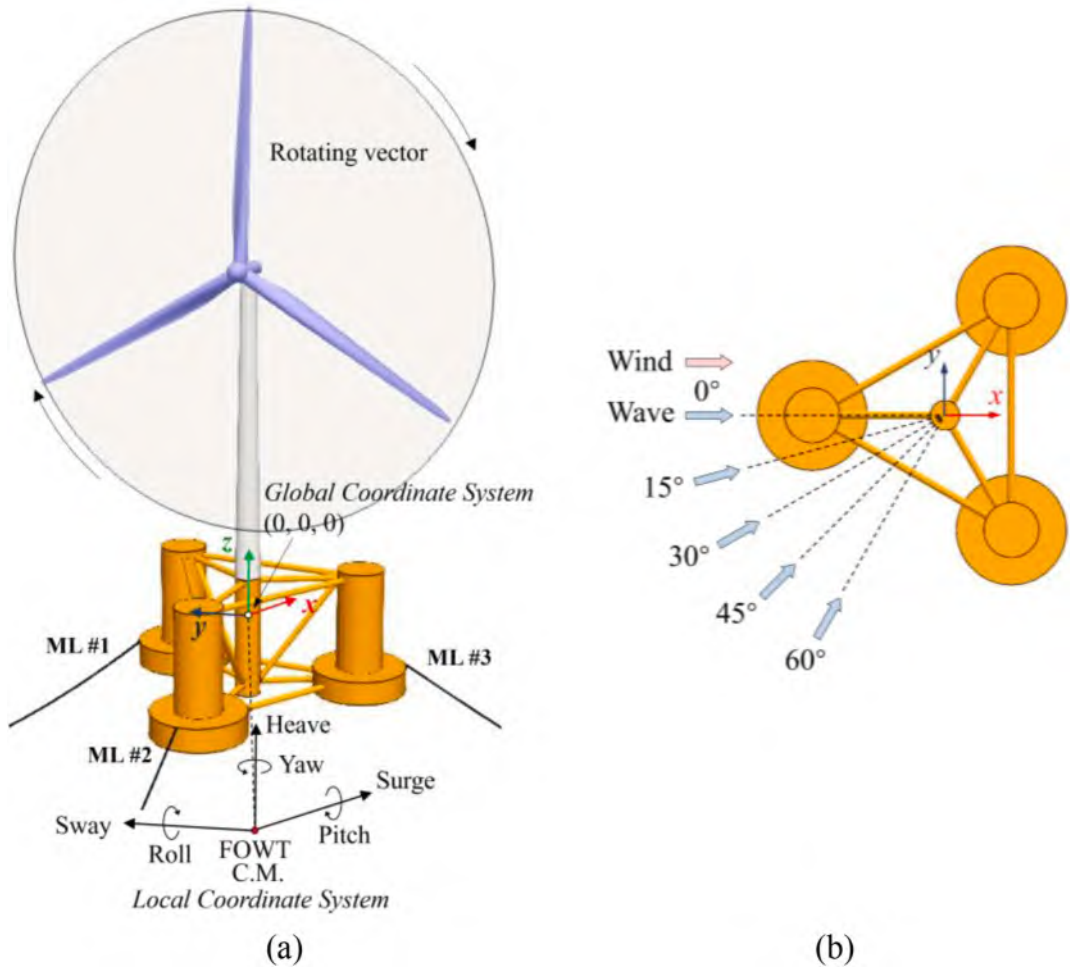

Fig. 7. Coordinate definitions: (a) global and local coordinate systems; (b) wind and wave directions.

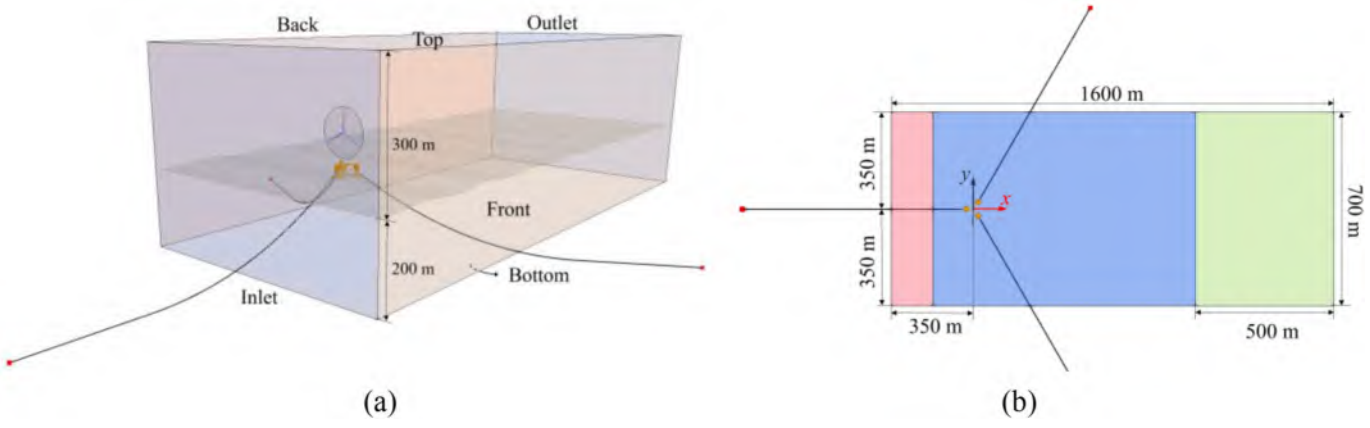

Fig. 8. Simulation domain of LC.1–LC.3 and LC.4.1 cases: (a) 3D view and boundary definition; (b) relaxation zone settings.

misalignment are non-negligible. Lyu et al. (2019) found that the maximum displacements and rotations in surge, heave, roll, pitch, and yaw all occurred at 90° misalignment for Spar-type FOWT. Ding et al. (2024) also discovered that high-frequency oscillation in surge and pitch motions intensify with the increasing relative angle between wind and wave directions. Further research by Ai et al. (2025) found that using a multi-segment mooring system using buoy and clump weights can reduce the impact of changes in wind and wave direction on platform motion response. Wang et al. (2022) reported that the maximum and main bearing fatigue damage of turbine peaked at 30°misalignment. Li et al. (2020) indicated that the wind-wave misalignment had little impact on power generation, but it significantly affected the platform motion and turbine structural loads. Using QBlade with FVW method, Muhammad et al. (2025) observed the most significant roll motion response at 90° misalignment, accompanied by significant wake fluctuations and power generation loss. However, these researches predominantly relied on FAST or other fast calculation software, which could not accurately resolve wake characteristics. In contrast, CFD

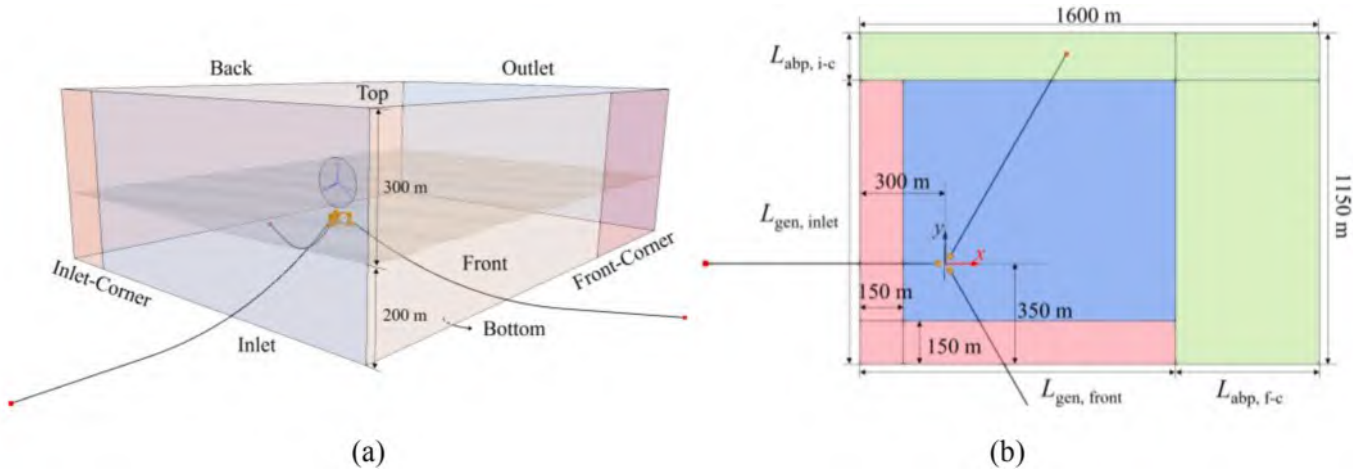

Fig. 9. Simulation domain of LC.4.2–LC.4.5 cases: (a) 3D view and boundary definition; (b) relaxation zone settings.

Table 3
Properties of LC.4.2 to LC.4.5 simulation domain.

Case	$L_{abp,\ i\text{-}c}$	$L_{gen,\ inlet}$	$L_{gen,\ front}$	$L_{abp,\ f\text{-}c}$
LC.4.2, Wave Dir. = 15°	166 m	984 m	1100 m	500 m
LC.4.3, Wave Dir. = 30°	253 m	897 m	1100 m	500 m
LC.4.4, Wave Dir. = 45°	324 m	826 m	1100 m	500 m
LC.4.5, Wave Dir. = 60°	382 m	758 m	1208 m	392 m

Table 4
Total cell number and grid size (Δx, Δy, Δz) of LC.1–LC.4 cases.

Case	Cell number	Near actuator points (m)	Near free surface (m)	Near FOWT platform (m)
LC.1, LC.2	2,666,862	(3, 3, 3)	(3, 3, 1)	(1.5, 1.5, 0.5)
LC.3.1	2,704,011	(15, 15, 15)	(1.875, 1.875, 0.8)	(0.469, 0.469. 0.200)
LC.3.2	5,337,890	(12, 12, 12)	(1.5, 1.5, 0.5)	(0.375, 0.375. 0.125)
LC.3.3	9,547,440	(10, 10, 10)	(1.25, 1.25, 0.4)	(0.156, 0.156, 0.050)
LC.4.1	9,187,454	(3, 3, 3)	(1.5, 1.5, 0.5)	(0.375, 0.375. 0.125)
LC.4.2–LC.4.5	10,598,072			

methods offer significant advantages. For example, in ship research, Nam et al. (2019) conducted CFD simulations to predict green water on an FPSO sidewall, and the results showed good agreement with physical experiments in capturing the overall process and relative wave motions. Liao et al. (2021) investigated the seakeeping performance of a trimaran, identifying significant slamming on the side hulls due to the combined effect of roll and heave motions under oblique waves, which generated noticeable splashes on the cross-deck. Furthermore, Fu et al. (2021) found that the large pitch motion of trimaran would appear at oblique stern waves, with further analysis showing the stability is much more sensitive at small wave-length conditions (wave-length/ship-length, $\lambda/L = 0.88$). Therefore, this study also adopts a CFD approach to analysis the wind-wave misalignment effects on the aero-hydrodynamic performance and wake characteristics of the floating offshore wind turbine. This approach intuitively reveals the turbine wake vortex structures and wake evolution, enabling wake deficit analysis and available power calculation for downstream turbines through time-averaged velocity fields, and provides a quantitative assessment of wake recovery.

This study presents a new wind generation and absorption module based on relaxation zone approach within the waves2Foam toolbox (Jacobsen, 2017), extending its capability from a uniform (zero-gradient) wind profile to include exponential and logarithmic shear wind profiles for coupled wind-wave simulations. The enhanced toolbox is subsequently coupled with the FOWT-UALM-SJTU solver to conduct fully coupled aero-hydrodynamic simulations of the NREL-5MW OC4 semi-submersible FOWT. These simulations systematically investigate the effects of wind-wave misalignment under regular wave conditions, considering five wave directions: 0°, 15°, 30°, 45°, and 60°. This paper is structured as follows: Section 2 details the numerical methods and developments; Section 3 describes the OC4 FOWT model and numerical settings; Section 4 presents various validations of FOWT-UALM-SJTU solver, along with UALM projection calibration and grid convergence; Section 5 discusses the hydrodynamics, aerodynamics, and wake characteristics under wind-wave misalignment (oblique wave) conditions. And the key findings are summarized in Section 6.

2. Numerical methods

FOWT-UALM-SJTU is an aero-hydro-servo-elastic coupled solver developed based on OpenFOAM. Its hydrodynamic core originates from our established naoe-FOAM-SJTU solver (Cao and Wan, 2014; Wang et al., 2019), which includes wave generation and 6 Degrees of Freedom (DoF) motion solving modules. Liu et al. (2015) further incorporated mooring modules into naoe-FOAM-SJTU, enabling tension calculations. Li et al. (2015) and Cheng et al. (2019) modified the SOWFA's ALM module to UALM module, developing the FOWT-UALM-SJTU solver for aero-hydrodynamic simulations, which also supports an active pitch angle and rotor speed control. Huang et al. (2020; 2024) implemented aeroelastic analysis of FOWT by introducing an equivalent beam theory into the UALM. Xu et al. (2024) achieved complex air-sea input at inlet boundary through precursor simulation methods, enabling turbine wake analysis under atmospheric boundary layer flows. In present study, waves2Foam is expanded and coupled for wind/wave generation, and the gravitational effects of blade and hub mass are incorporated into UALM. While, the aeroelastic effects are disregarded to simplify the modeling. The overall framework of this solver is illustrated in Fig. 1.

2.1. Governing equations

In CFD simulations based on OpenFOAM, the incompressible viscous governing equations comprise the continuity equation and momentum equation, expressed as:

$$\nabla\cdot\mathbf{U} = 0 \tag{1}$$

$$\frac{\partial\rho\mathbf{U}}{\partial t} + \nabla\cdot\left(\rho(\mathbf{U}-\mathbf{U}_g)\mathbf{U}\right) = -\nabla \mathrm{p}_d - \mathbf{g}\cdot\mathbf{x}\nabla\rho + \nabla\left(\mu_{eff}\nabla\mathbf{U}\right) + \nabla\mu_{eff}\nabla\mathbf{U} + \mathbf{f}_\sigma + \mathbf{f}_\varepsilon \tag{2}$$

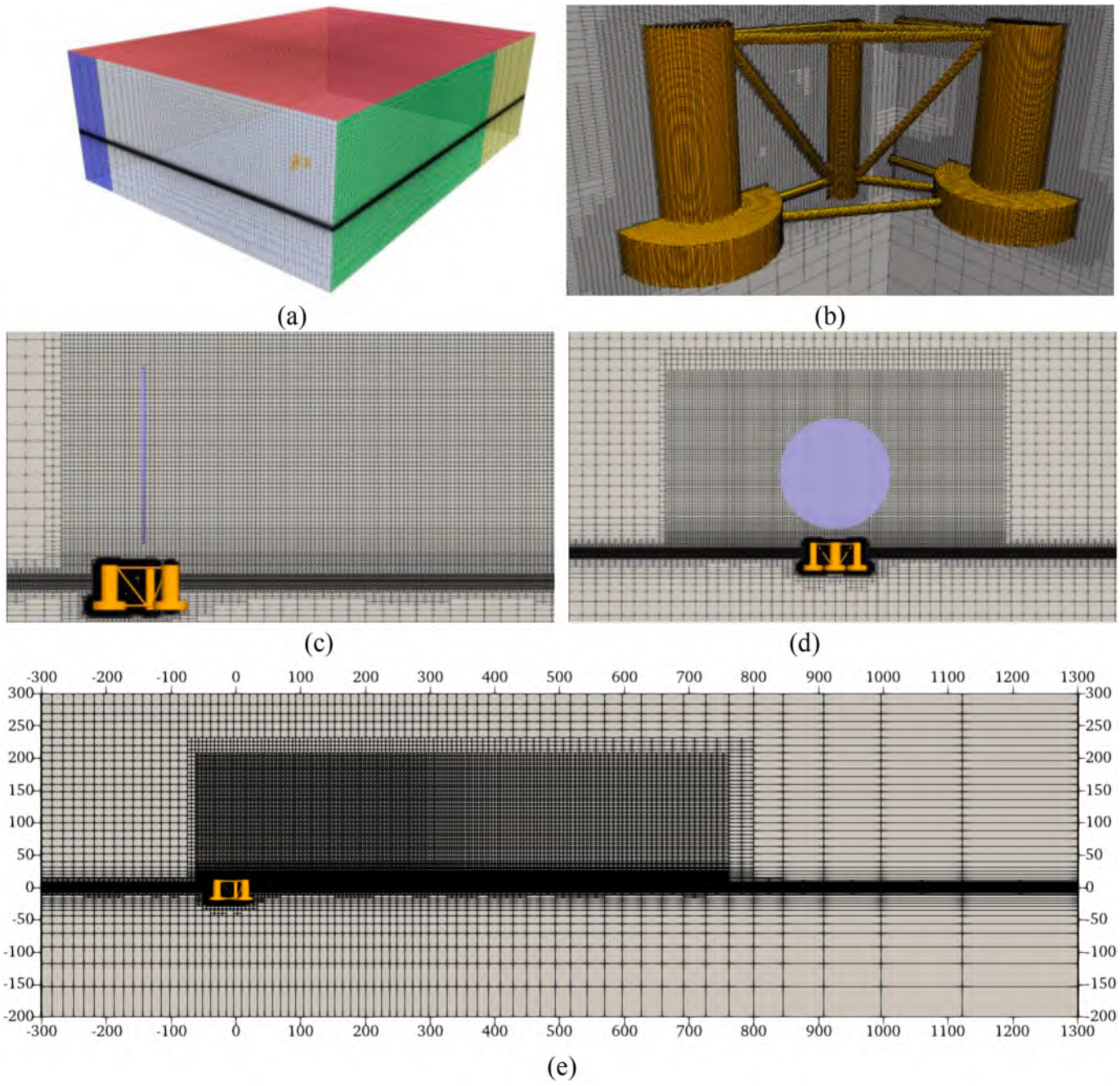

Fig. 10. Mesh distribution of LC.4.2–LC.4.5 cases: (a) full grid domain; (b) grid near the platform; (c) grid on the *xoz*-plane; (d) grid on the *yoz*-plane; (e) grid of the turbine wake region.

Table 5
B.C.s of LC.1–LC.4 cases (*pIOV: pressureInletOutletVelocity).

(a)LC.1–LC.3, LC.4.1 cases					
Boundary condition	Inlet/Outlet	Front/Back	Top	Bottom	Inlet-Corner/Front-Corner
Dynamic pressure	zeroGradient	symmetryPlane	totalPressure	slip	–
Velocity	waveVelocity	symmetryPlane	pIOV*	slip	–
Volume fraction	waveAlpha	symmetryPlane	inletOutlet	zeroGradient	–
(b) LC.4.2–LC.4.5 cases					
Boundary condition	Inlet/Outlet	Front/Back	Top	Bottom	Inlet-Corner/Front-Corner
Dynamic pressure	zeroGradient	zeroGradient	totalPressure	slip	zeroGradient
Velocity	waveVelocity	waveVelocity	pIOV*	slip	waveVelocity
Volume fraction	waveAlpha	waveAlpha	inletOutlet	zeroGradient	waveAlpha

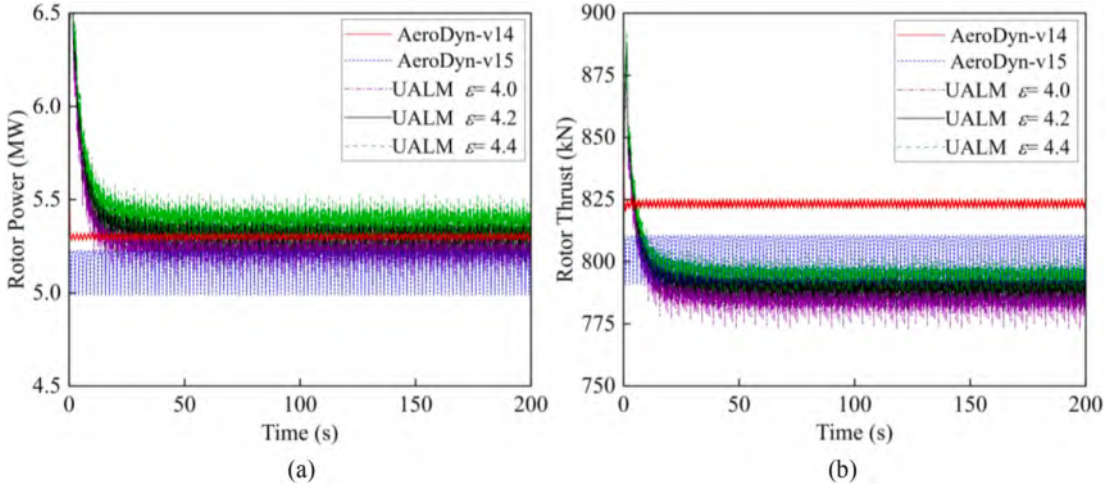

Fig. 11. Aerodynamic comparison with ε (Cases LC.1.1–LC1.3): (a) rotor thrust; (b) rotor power.

Table 6
Mean value of aerodynamic comparison for LC.1.1–LC1.3 cases.

Aerodynamic responses		AeroDyn-v14	AeroDyn-v15	UALM ε = 4.0	UALM ε = 4.2	UALM ε = 4.4
Rotor power (MW)	Mean	5.303	5.175	5.253	5.347	5.430
	Diff.	–	−2.41%	−0.94%	0.83%	2.39%
Rotor thrust (kN)	Mean	823.296	806.122	786.515	791.917	796.664
	Diff.	–	−1.86%	−4.47%	−3.81%	−3.23%

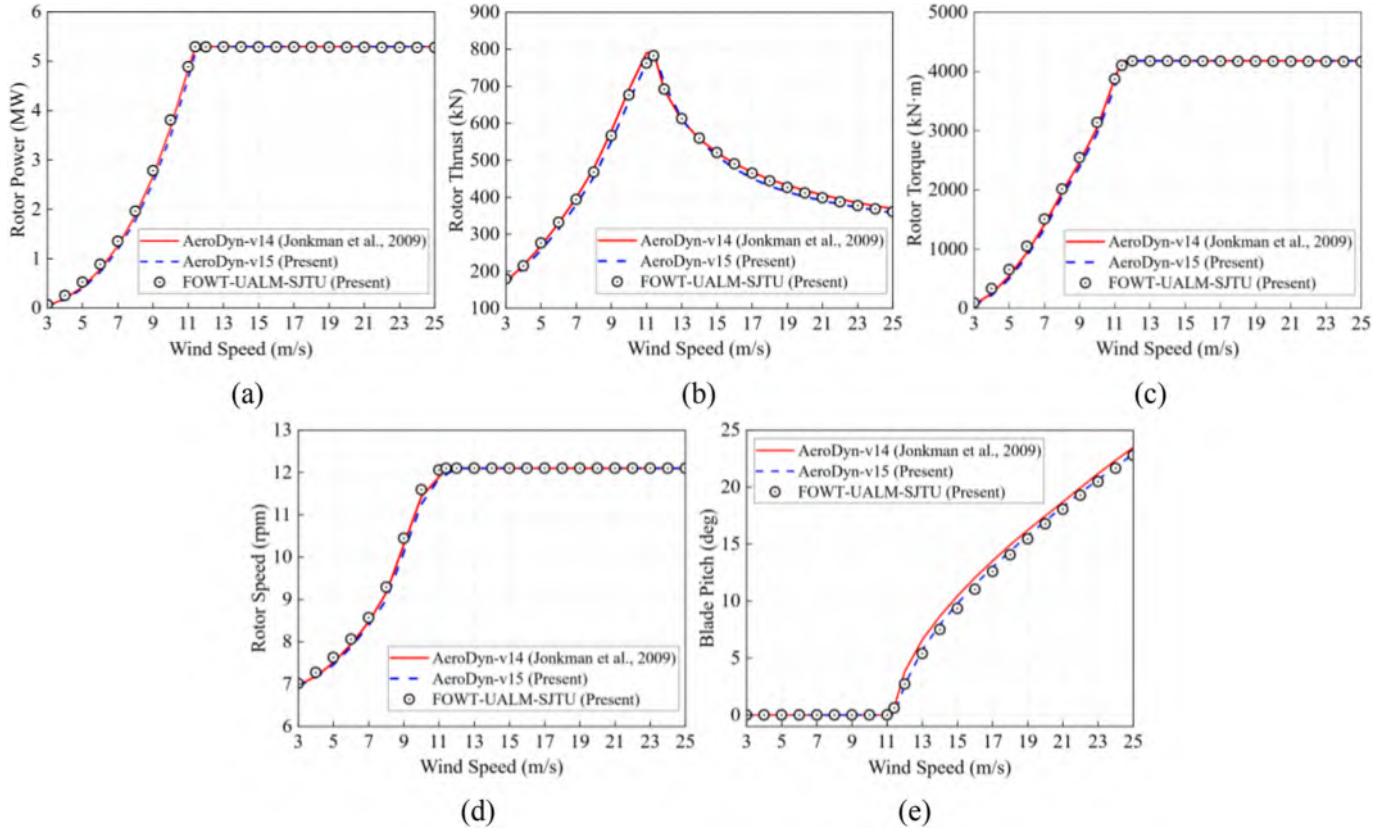

Fig. 12. Steady aerodynamic comparison in different wind speeds (Cases LC.1.4–LC1.2): (a) rotor power; (b) rotor thrust; (c) rotor torque; (d) rotor speed; (e) blade pitch.

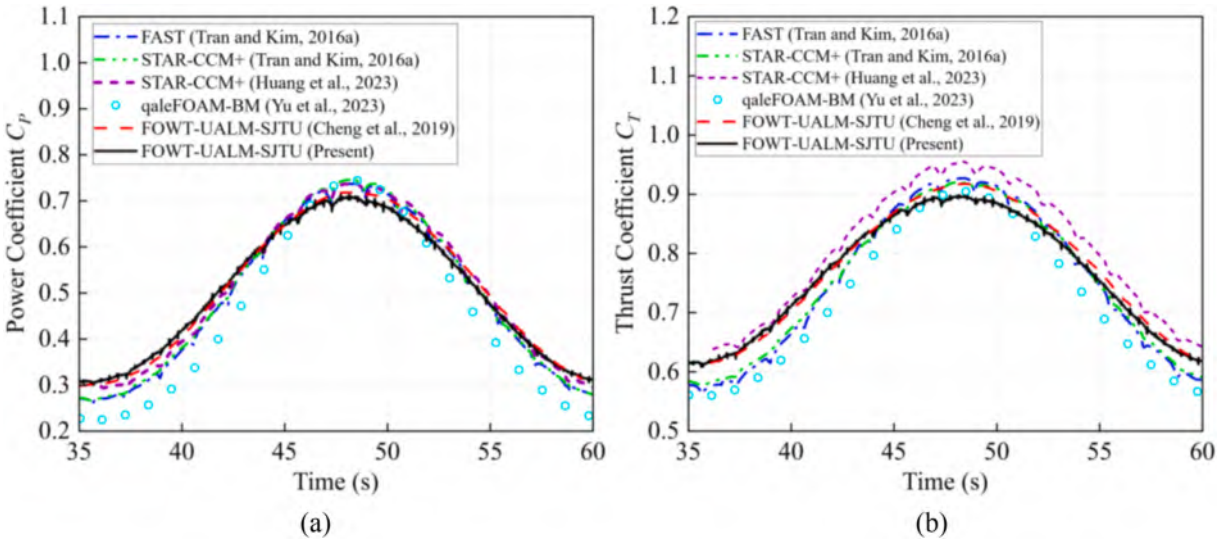

Fig. 13. Unsteady aerodynamic comparison under a prescribed surge motion (Case LC.1.2): (a) power coefficient C_P; (b) thrust coefficient C_T.

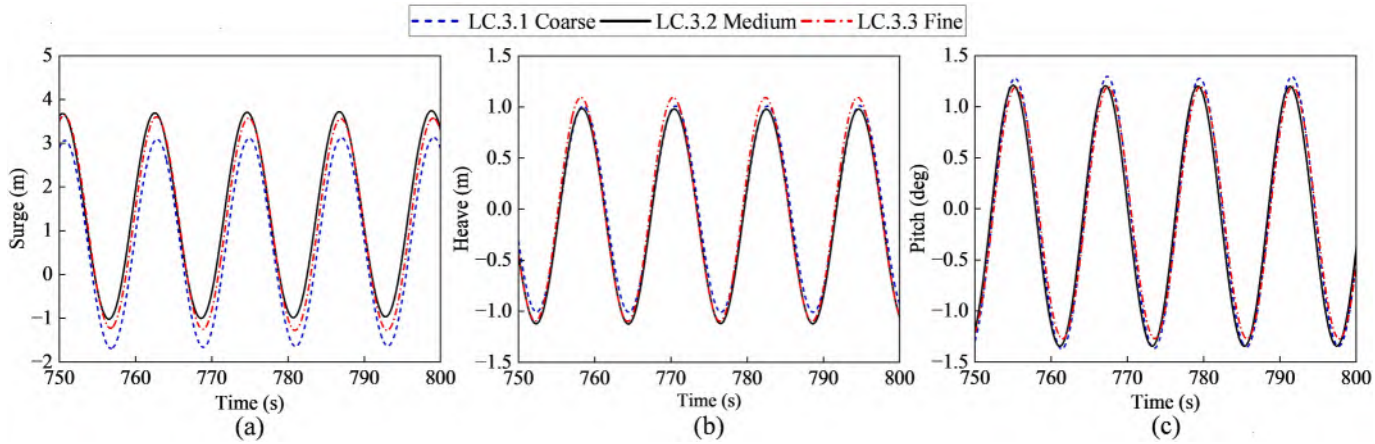

Fig. 14. 3DoF motion responses comparison with different cell size (Cases LC.3.1–LC.3.3): (a) surge motion; (b) heave motion; (c) pitch motion.

Table 7
Hydrodynamic responses P2P Amp. in hydrodynamic validation.

Hydrodynamic responses	Exp (Coulling et al., 2013)	FAST (Coulling et al., 2013)	STAR-CCM+ (Tran and Kim, 2016b)	STAR-CCM+ (Huang et al., 2023)	OpenFOAM (Haider et al., 2024)	MRFoam (Cai et al., 2025)	OpenFAST (Present)	FOWT-UALM-SJTU (Present)
Surge (m)	4.428	4.266	4.632	4.180	4.298	4.274	4.346	4.702
Heave (m)	2.308	1.832	1.896	2.058	1.902	1.842	2.142	2.018
Pitch (deg)	1.972	1.974	2.296	1.910	1.796	1.716	2.574	2.564
ML #1 tension (kN)	205.782	99.858	103.284	88.022	161.984	115.126	207.726	152.928
ML #2 tension (kN)	615.270	205.782	216.568	192.122	428.952	348.604	505.302	574.256

where, $\mathbf{U}$ and $\mathbf{U}_g$ represent the velocity of flow field and grid nodes, respectively; ρ is the flow density; $p_d = p - \rho \mathbf{g}\mathbf{x}$ denotes the dynamic pressure, in which p is the total pressure; $\mathbf{g}$ is the gravitational acceleration; $\mathbf{x}$ is the position vector; $\mu_{eff} = \rho(\nu + \nu_t)$ is the effective dynamic viscosity coefficient, in which ν are ν_t are the kinematic and turbulent eddy viscosity; $\mathbf{f}_\sigma$ and $\mathbf{f}_\varepsilon$ are the source terms of surface tension and turbine body forces, respectively. Besides, the Delayed Detached Eddy Simulation (DDES) turbulence model is adopted (Xue et al., 2024).

2.2. Free surface modeling

The air-water free surface is captured by the VOF method (Hirt and Nichols, 1981), which defines a volume fraction α_v to represent the proportion of each fluid in one cell. The volume fraction α_v, fluid densities ρ and fluid viscosities μ are defined as follows,

$$\begin{cases} \alpha_v = 0, air \\ 0 < \alpha_v < 1, free\ surface \\ \alpha_v = 1, water \end{cases} \tag{3}$$

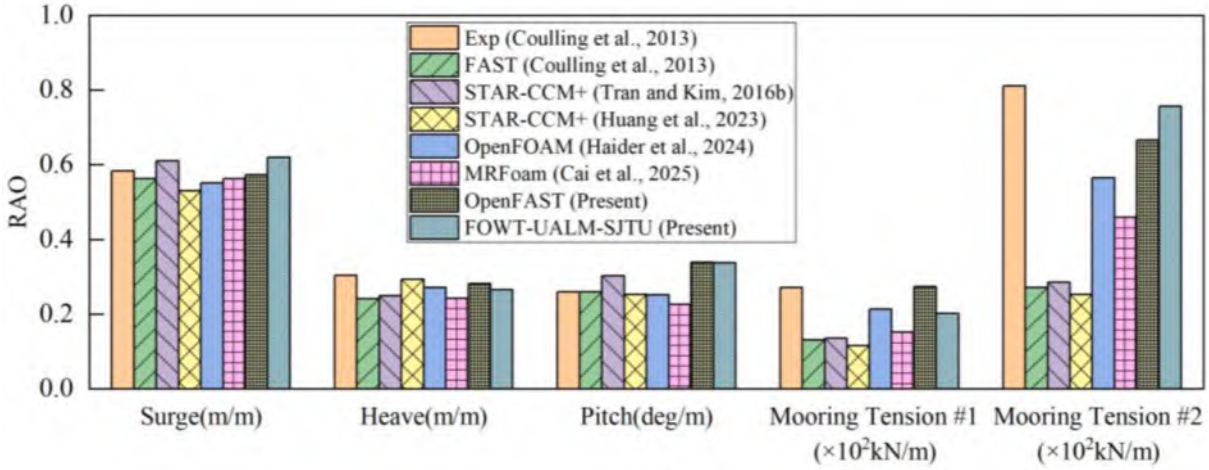

Fig. 15. RAO comparison (RAO = P2P Amp./wave height).

$$\rho = \alpha_v \rho_{\text{water}} + (1-\alpha_v)\rho_{\text{air}} \tag{4}$$

$$\mu = \alpha_v \mu_{\text{water}} + (1-\alpha_v)\mu_{\text{air}} \tag{5}$$

The transport equation of volume fraction is governed by:

$$\frac{\partial \alpha_v}{\partial t} + \nabla\cdot(\alpha_v \mathbf{U}) + \nabla\cdot(\alpha_v(1-\alpha_v)\mathbf{U}_r) = 0 \tag{6}$$

where, $\mathbf{U}_r = \mathbf{U}_{\text{water}} - \mathbf{U}_{\text{air}}$ is an artificial compression velocity applied to sharped the interface. And the surface tension source term $\mathbf{f}_\sigma$ in Eq. (2) is modeled as,

$$\mathbf{f}_\sigma = \sigma\kappa\nabla\alpha_v \tag{7}$$

where, σ is the surface tension coefficient, and κ is the interface curvature.

2.3. Wave generation and absorption

The open-source toolbox waves2Foam (Jacobsen, 2017) is coupled with FOWT-UALM-SJTU solver. This toolbox could utilize the relaxation zone technique for wave generation and absorption. Within this zone, the fluid velocity **U** and volume fraction α_v are blended with theoretical values, which can be expressed as,

$$\phi = (1-\omega_R)\phi_{\text{target}} + \omega_R \phi_{\text{computed}} \tag{8}$$

where, ϕ represents the relaxed value of **U** or α_v, ϕ_{target} is the target (theoretical) value, and ϕ_{computed} is the computational value at current time step; $\omega_R \in [0,1]$ is a weight parameter. In this study, ω_R is computed using the exponential form (Hu et al., 2016; Jacobsen, 2017):

$$\omega_R = 1 - \frac{\exp(\sigma^p) - 1}{\exp(1) - 1} \tag{9}$$

where, the exponent p is set to the default value of 3.5; σ is a normalized distance function defining the local position within the relaxation zone. The relationship between ω_R and σ is illustrated in Fig. 2. Besides, waves2Foam provide waveVelocity and waveAlpha boundary conditions (B.C.s) for **U** and α_v boundaries. This study employs second-order Stokes regular wave for simulation.

2.4. Wind generation and absorption

Since original waves2Foam only supports one single-speed uniform wind profile, this study implements a new windTheories base class within the waves2Foam module (libwaves2foam.so), enabling the generation of uniform (non-shear), exponential, and logarithmic shear wind profiles through relaxation zone method. The code modifications involve the original fvPatchField, relaxationZone, setWaveField and waveTheory class. The new file structure is shown in Fig. A.1 (Appendix A). The exponential shear wind type is applied in this study, which can be expressed as,

$$U_{\text{wind,exp}}(z) = \begin{cases} U_{\text{ref}} \times \left(\dfrac{z-\eta}{H_{\text{ref}}}\right)^{\alpha}, z-\eta \geq H_b \\ U_{\text{ref}} \times \left(\dfrac{H_b}{H_{\text{ref}}}\right)^{\alpha} \times \dfrac{z-\eta}{H_b}, z-\eta < H_b \end{cases} \tag{10}$$

where, U_{ref} is a reference wind speed at the reference height H_{ref}; z is the vertical coordinate; η is the wave surface evaluation; H_b is a parameter that represents a certain height above the free surface, set to 10 m; α is the exponential factor, set to 0.143. To avoid excessive slope of shear wind, the wind profile is applied a linear distribution below H_b. Besides, the validation of shear wind generation is shown later in Fig. 17.

2.5. Aerodynamic modeling

The ALM method discretizes the wind turbine blade into a series of actuator points (Sørensen and Shen, 2002). Compared to traditional blade-resolved mesh method, ALM method offers faster computation speed and requires fewer grid cells, making it particularly suitable for wind turbine wake research. The UALM extends the traditional ALM by accounting for platform-induced motion effects, including changes in actuator point displacement, relative velocity (from $\mathbf{U}'_{\text{rel}}$ to $\mathbf{U}_{\text{rel}}$), and angle of attack (from α' to α) (Cheng et al., 2019), as illustrated in Fig. 3. The relative wind velocity $\mathbf{U}_{\text{rel}}$, attack angle α and sectional aerodynamic force $\mathbf{F}_{\text{total}}$ can be expressed as,

$$\mathbf{U}_{\text{rel}} = \mathbf{U}_{\text{wind}} + \mathbf{U}_{\text{rotor}} + \mathbf{U}_{\text{motion}} \tag{11}$$

$$\alpha = \varphi - \beta \tag{12}$$

$$\beta = \theta_{\text{pitch}} + \theta_{\text{twist}} \tag{13}$$

$$\mathbf{F}_{\text{total}} = \mathbf{F}_L + \mathbf{F}_D = \frac{1}{2}\rho \mathbf{U}_{\text{rel}}^2 (C_L \mathbf{e}_L + C_D \mathbf{e}_D) c dr \tag{14}$$

where, $\mathbf{U}_{\text{wind}}$ is the wind velocity; $\mathbf{U}_{\text{rotor}} = -\boldsymbol{\Omega} \times \mathbf{r}$ is the rotating blade velocity, with $\boldsymbol{\Omega}$ being the rotating angular velocity and $\mathbf{r}$ being the radial vector from the rotor shaft; $\mathbf{U}_{\text{motion}}$ is the platform-induced velocity; φ is the inflow angle relative the rotor plane; θ_{pitch} is the local blade pitch angle; θ_{twist} is the blade twist angle; $\mathbf{F}_L$ and $\mathbf{F}_D$ are the lift and

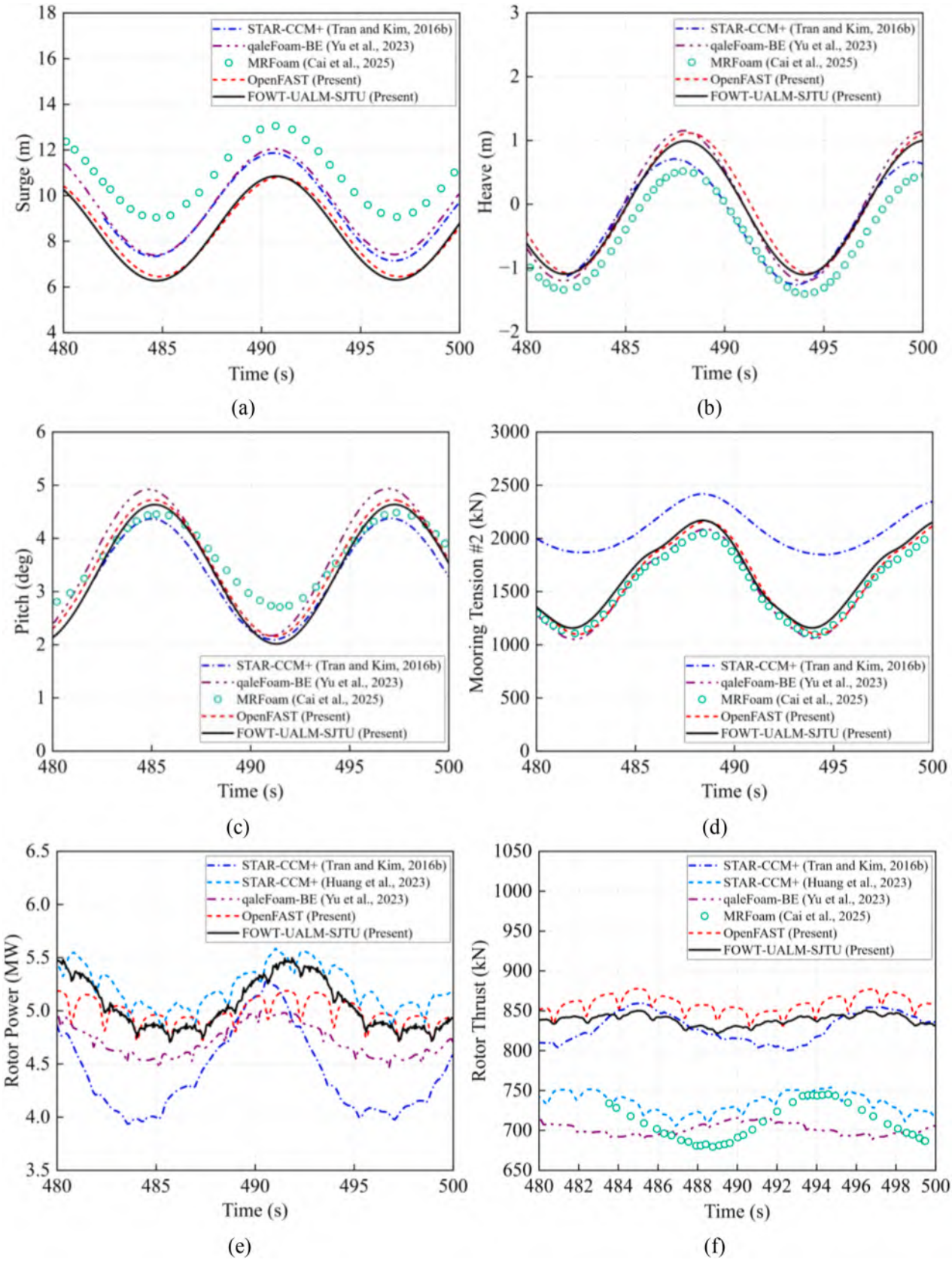

Fig. 16. Aero-hydrodynamic responses comparison in fully coupled validation (Case LC.4.1): (a) surge motion; (b) heave motion; (c) pitch motion; (d) ML #2 tension; (e) rotor power; (f) rotor thrust.

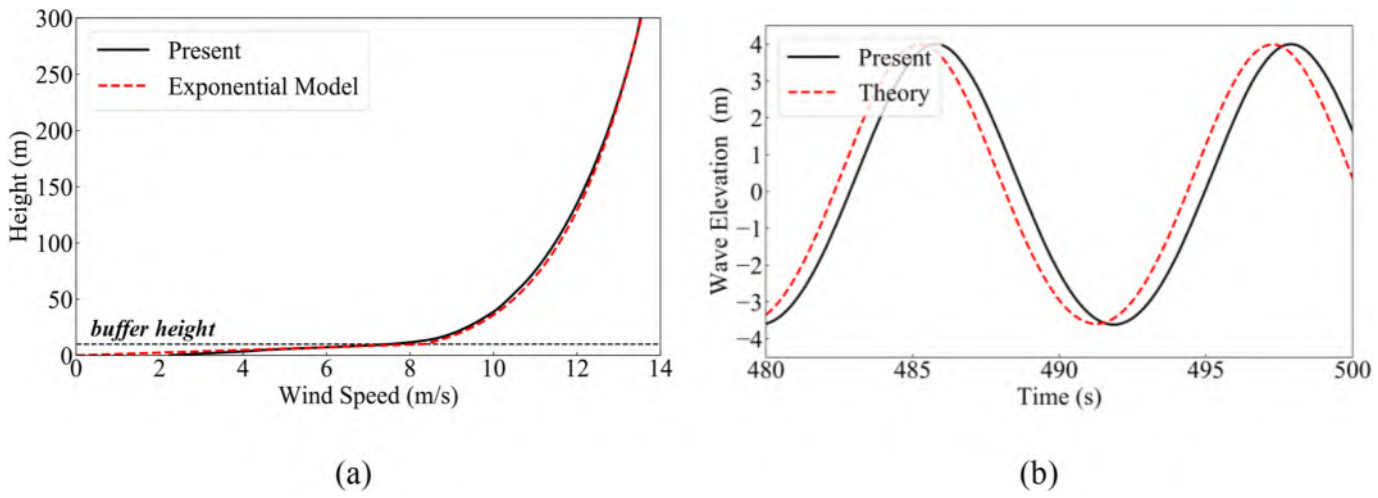

Fig. 17. Wind and wave generation validation: (a) shear wind profile; (b) wave elevation.

Table 8
Aero-hydrodynamic responses P2P Amp. and average in fully coupled validation (Case LC.4.1).

Dynamic responses		STAR-CCM+ (Tran and Kim, 2016b)	STAR-CCM+ (Huang et al., 2023)	qaleFoam-BE (Yu et al., 2023)	MRFoam (Cai et al., 2025)	OpenFAST (Present)	FOWT-UALM-SJTU (Present)
Surge (m)	Amp.	4.500	4.020	4.669	4.503	4.353	4.543
	Average	9.620	–	9.764	11.120	8.633	8.581
Heave (m)	Amp.	1.950	2.230	2.336	1.842	2.194	2.094
	Average	−0.260	–	–	−0.430	0.019	0.056
Pitch (deg)	Amp.	2.270	1.920	2.786	1.743	2.567	2.620
	Average	3.240	–	3.551	3.610	3.441	3.327
ML #2 tension (kN)	Amp.	562	–	1038	944	1060	1015
	Average	2134	–	1572	1578	1629	1666
Rotor power (MW)	Amp.	1.341	0.606	0.545	–	0.473	0.790
	Average	4.616	5.292	4.749	–	4.951	5.106
Rotor thrust (kN)	Amp.	59.209	35.180	27.460	64.900	47.994	32.585
	Average	829.953	736.260	702.970	711.950	853.758	834.961

drag forces; C_L and C_D are the lift and drag coefficients; ρ is air density; $\mathbf{e}_L$ and $\mathbf{e}_D$ are the unit vector in lift and drag directions; c is the chord length; dr is the segment spanwise length.

The body force source term $\mathbf{f}_\varepsilon$ representing the turbine's aerodynamic effect is given by,

$$\mathbf{f}_\varepsilon(x,y,z) = \sum_{i=1}^{N_b}\sum_{j=1}^{N_{p,i}} \mathbf{F}_{\text{total}}\left(x_{i,j},y_{i,j},z_{i,j}\right)\eta_\varepsilon\left(d_{i,j}\right) \tag{15}$$

where, N_b is the number of blades; $N_{p,i}$ is the number of actuator points; (x,y,z) is the field point position in global coordinate system, and $\left(x_{i,j}, y_{i,j}, z_{i,j}\right)$ is the actuator point position; $\eta_\varepsilon\left(d_{i,j}\right)$ is the regularization kernel function; ε is the projection width factor. More details could be referred to Sørensen and Shen's (2002) work.

Refer the works by Tran and Kim (2016a, 2016b) and web of NREL Forum (2025), the rotor thrust T_{thrust} is the superposition of aerodynamic force and structure forces along the turbine shaft, as shown in Fig. 4. Thus, in present study, the T_{thrust} is modified by followings,

$$T_{\text{thrust}} = \left(\mathbf{F}_{\text{aero}} + \sum_{i=1}^{N_b}\left(\mathbf{I}_{\text{blade},i} + \mathbf{G}_{\text{blade},i}\right) + \mathbf{I}_{\text{hub}} + \mathbf{G}_{\text{hub}}\right)\cdot\mathbf{e}_{\text{shaft}} \tag{16}$$

where, $\mathbf{F}_{\text{aero}}$ is the aerodynamic force by UALM method; $\mathbf{G}_{\text{blade}}$ and $\mathbf{G}_{\text{hub}}$ represent the gravitational forces of one single blade and hub; $\mathbf{I}_{\text{blade},i}$ and $\mathbf{I}_{\text{hub}}$ denote the inertial forces arising from platform motion and rotor rotation; $\mathbf{e}_{\text{shaft}}$ is the unit vector along shaft direction. Due to the complex causes of inertial forces and their small values under operating conditions, present work haven't considered these.

2.6. Mooring system modeling

The Lumped-Mass Method (LMM) is implemented in the solver to compute mooring tension, which is a dynamic calculation method that accounts for the inertial forces of mooring lines. This method discretizes the mooring line into N+1 mass nodes connected by N massless spring segments (Liu et al., 2015), as illustrated in Fig. 5 (a). In contrast to the spring method, by incorporating Morison's equation, the force equilibrium equation for node i, as shown in Fig. 5 (b), can be expressed as:

$$M_i\mathbf{a}_i = \mathbf{F}_{Ti} + \mathbf{F}_{Ti-1} + \mathbf{F}_{Di} + \mathbf{F}_{Ai} + \mathbf{W}_i \tag{17}$$

where, $M_i = (m_i + m_{i-1})/2$ is the equivalent mass; m_i is the segment mass; $\mathbf{a}_i$ is the node acceleration; $\mathbf{F}_{Ti}$ is the spring segment tension; $\mathbf{W}_i = (0,0,-M_i\mathbf{g})$ is the gravitational force; $\mathbf{F}_{Di}$ and $\mathbf{F}_{Ai}$ are the drag forceand added mass force. More details could be referred to Liu's work (2015; 2019b).

3. OC4 FOWT model and numerical settings

3.1. OC4 FOWT model

The OC4 FOWT is a semi-submersible FOWT, which could be divide into three parts: NREL-5MW wind turbine (Jonkman et al., 2009), OC4 floating platform and three-line mooring system (Robertson et al., 2014), as shown in Fig. 6. Main properties of each component are summarized in Table A.1 (Appendix A). Due to the lack of the overall mass, center of mass (C.M.) and moment of inertia provided by NREL, the values of those overall properties used in CFD are listed in Table 1.

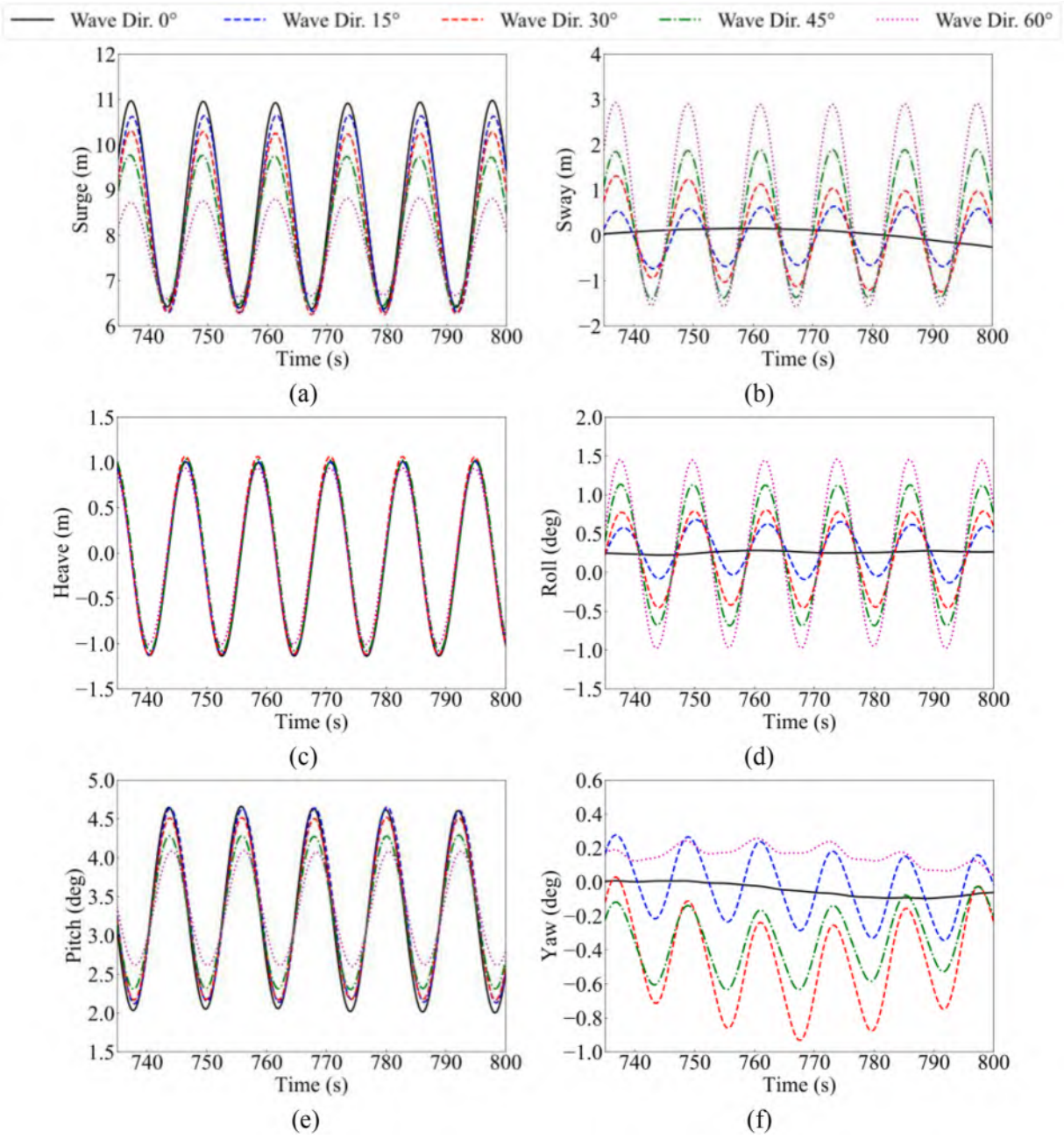

Fig. 18. 6DoF motion responses in last five wave periods: (a) surge motion; (b) sway motion; (c) heave motion; (d) roll motion; (e) pitch motion; (f) yaw motion.

For the mooring system, the OC4 design document (Robertson et al., 2014) specifies the hydrodynamic drag and added-mass coefficients: $C_D = 1.1$ and $C_A = 1.0$. However, OpenFAST and MoorDyn apply different values in their official tests: $C_{DN} = 2.0$, $C_{DT} = 0.4$, $C_{AN} = 0.8$, $C_{AT} = 0.25$. The parameter N and T represent the transverse and tangential directions, respectively. Present work adopts the OpenFAST's settings.

3.2. Case conditions

There are three case sets for validations and one case set for wind-wave misalignment analysis. (1) The first set LC.1 involves three cases LC.1.1–LC.1.3 for calibration of UALM projection width factor with $\varepsilon =$ 4.0, 4.2, 4.4 under rated wind speed and twenty-four cases LC.1.4–LC.1.27 for validations of steady aerodynamic performance under 3–25 m/s. (2) The second set LC.2 is unsteady aerodynamic validation, simulating the forced motion of FOWT in surge direction, following the sine function $x = A\sin(\omega t)$. In which, the amplitude $A = 8$ m, and the angular velocities $\omega = 0.246$ rad/s. (3) The third set LC.3.1–LC.3.3 involves grid convergence analysis with three different types of mesh distribution under Stokes 2nd-order regular wave with wave height $H = 7.58$ m, wave period $T = 12.1$s, water depth $h = 200$ m, being used for hydrodynamic validations. (4) The fourth set LC.4.1–LC.4.5 involves wind-wave misalignment cases under 0° shear wind with 11.4 m/s (at $z = 90$ m) and five different wave directions (0°, 15°, 30°, 45°, 60°) with $H = 7.58$ m, $T = 12.1$s, $h = 200$ m. Besides, the LC.4.1 case is also used for fully coupled verification. The wind speed for all case sets is 0°. More settings are listed in Table 2. The Stokes 2nd-order wave model is adopted because the ratio H/gT^2-h/gT^2 falls within the most applicable range of Stokes 2nd-order wave theory (Holthuijsen, 2010; Claus and López, 2022). And turbulent wind is not considered in any cases.

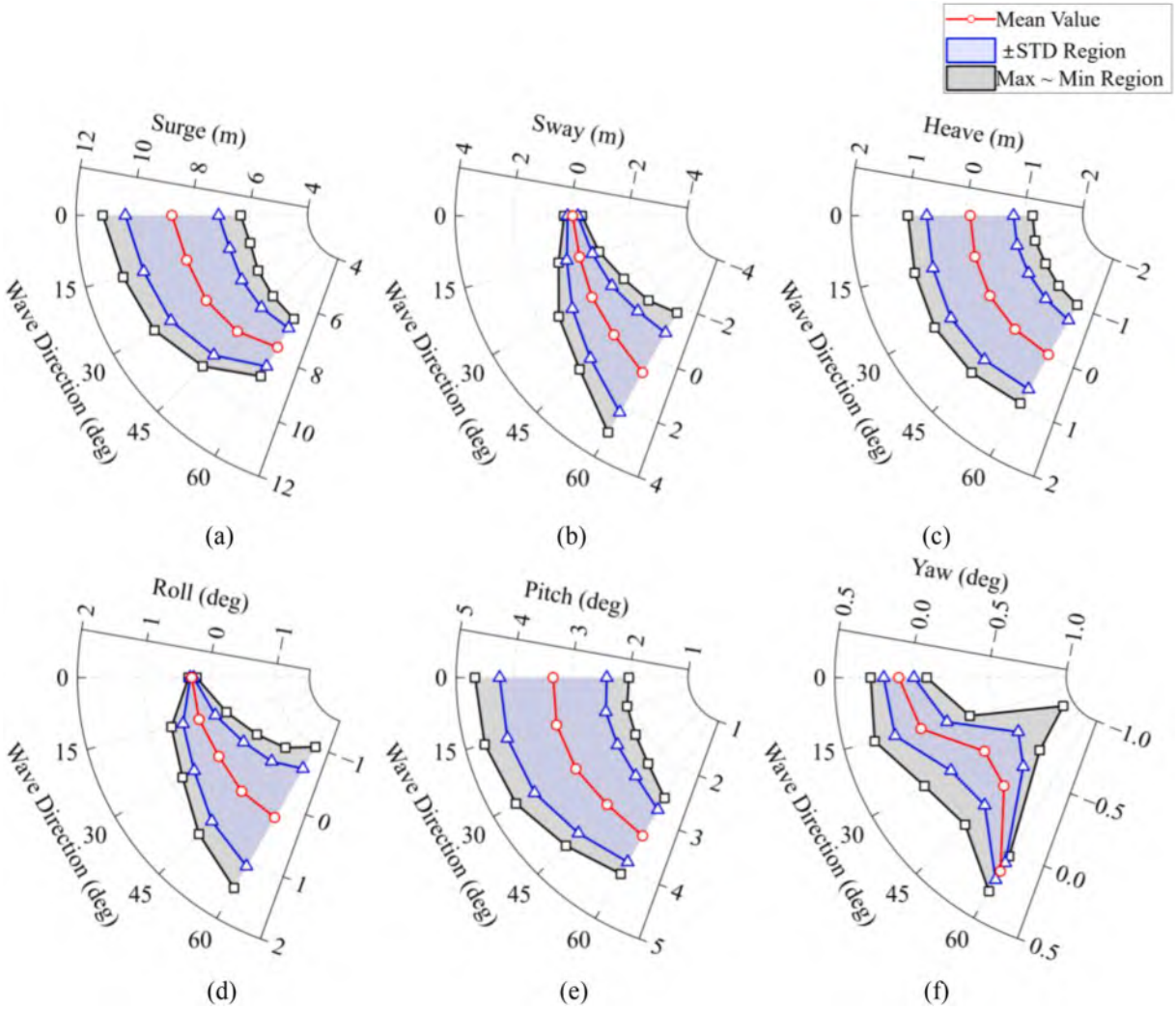

Fig. 19. Max-minimum region, mean value and STD region of hydrodynamic motion responses: (a) surge motion; (b) sway motion; (c) heave motion; (d) roll motion; (e) pitch motion; (f) yaw motion.

Table 9
Mean value of hydrodynamic responses.

Hydrodynamic motion responses	LC.4.1, Wave Dir. = 0°	LC.4.2, Wave Dir. = 15°	LC.4.3, Wave Dir. = 30°	LC.4.4, Wave Dir. = 45°	LC.4.5, Wave Dir. = 60°
Surge (m)	8.684	8.379	8.283	8.078	7.668
Sway (m)	−0.059	−0.110	0.022	0.213	0.650
Heave (m)	−0.059	−0.050	−0.028	−0.021	−0.024
Roll (deg)	0.271	0.246	0.183	0.230	0.241
Pitch (deg)	3.325	3.373	3.353	3.302	3.357
Yaw (deg)	0.084	−0.016	−0.344	−0.306	0.151

3.3. Computational domain

The global coordinate system is defined at the intersection of the center column centerline and SWL, and the local coordinate system is fixed at FOWT C.M., as shown in Fig. 7 (a). In the local coordinate system, the motion along the x, y, z is defined as surge, sway and heave. The motions around these axes are roll, pitch and yaw, following the right-handed rule. The directions of wind and wave are defined as shown Fig. 7 (b).

The simulation domain of the validation cases from LC.1–LC.4.1 measures 1500 m (x) × 440 m (y) × 500 m (z), as shown in Fig. 8. The red zones represent the INLET-type relaxation zones for wind-wave generation, and the green zones represent the OUTLET-type zones for absorption. While, in the wind-wave misalignment cases from LC.4.2–LC.4.5, the domain is expanded to 1600 m (x) × 1150 m (y) × 500 m (z), as shown in Fig. 9. Compared to Fig. 8, the boundaries of inlet and front which used for oblique wave generation are cut to construct two corner boundaries, avoiding wave reflection of different forms of boundary conditions. More lengths of LC.4.2–LC.4.5 boundary and relaxation zone are list in Table 3.

3.4. Mesh distribution

The total cell count and grid size across distinct regions for LC.1–LC.4 cases are summarized in Table 4. Three mesh resolutions, corresponding to coarse, medium, and fine, respectively, are employed in the LC3 cases for the hydrodynamic mesh convergence analysis. Although the gird configurations vary among cases, equivalent resolution is maintained in critical regions of interest. LC.4.1–LC.4.5 cases adopt the mesh refinement strategy near the actuator points from LC.1–LC.2 cases, as well as the refinement near the free surface and FOWT platform from LC.3.2 case, as shown in Fig. 10. The difference lies only in the size of

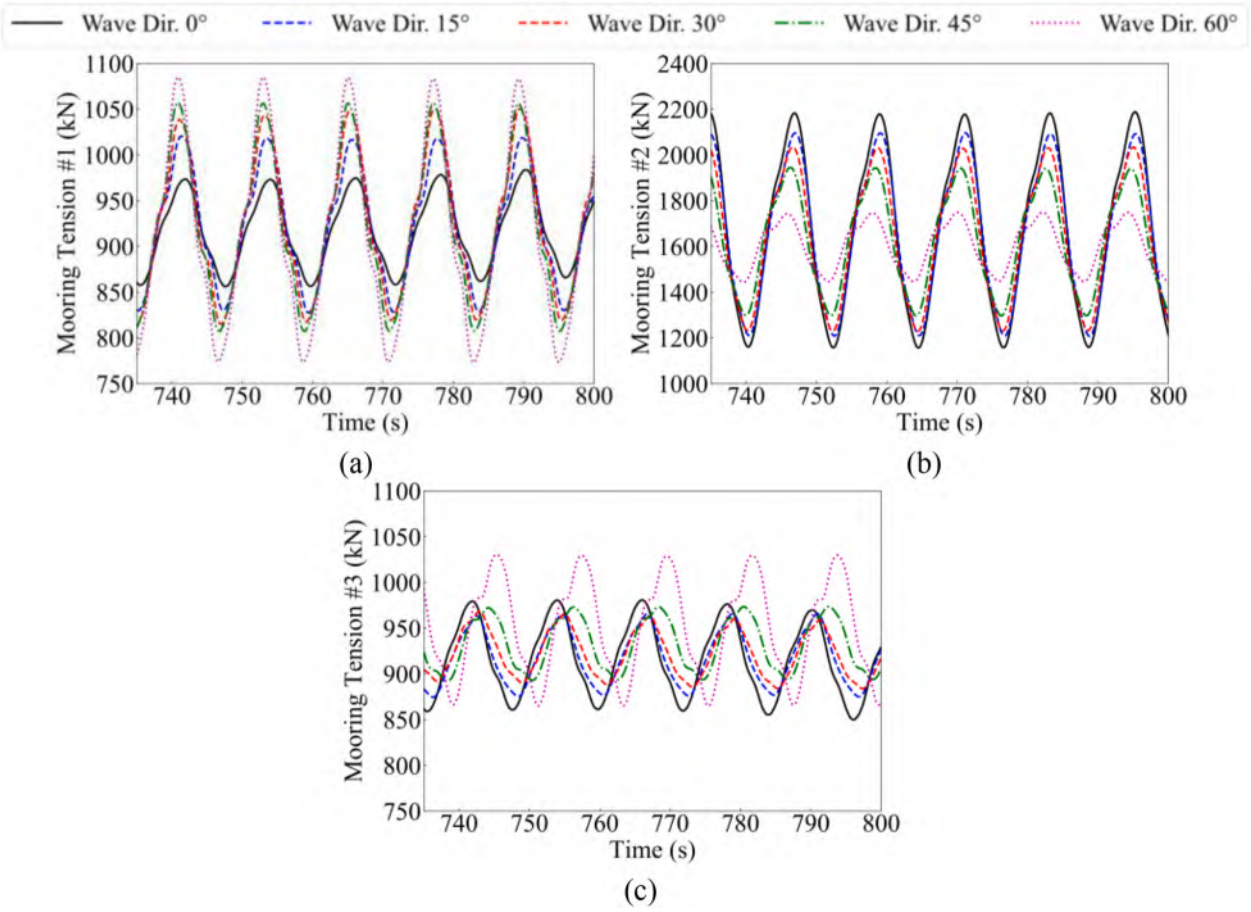

Fig. 20. Mooring responses: (a) tension of ML #1; (b) tension of ML #2; (c) tension of ML #3.

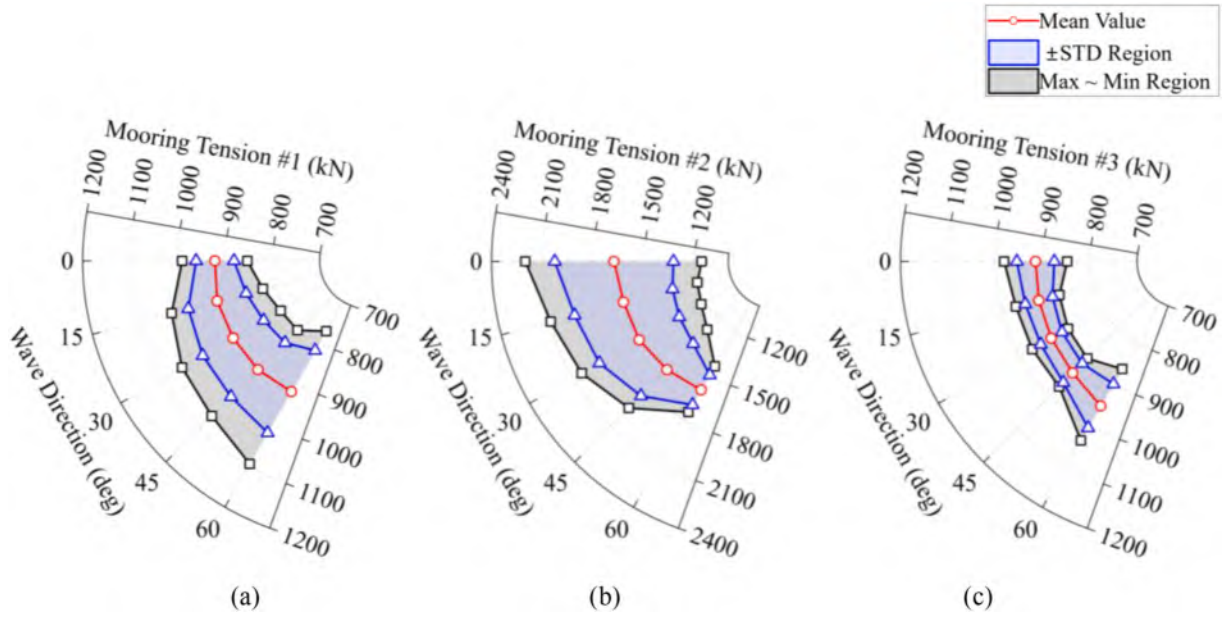

Fig. 21. Max-minimum value region, mean value and STD region of mooring tension: (a) ML #1 tension; (b) ML #2 tension; (c) ML #3 tension.

simulation domain and division of boundaries.

The simulations for all cases presented in this study were conducted on the Siyuan-1 cluster at the High Performance Computing Center of Shanghai Jiao Tong University. The CPU configuration is dual Intel Xeon ICX Platinum 8358 processors (32 cores, 2.6 GHz). The core count for each case was configured to maintain a resolution of approximately 5000–10,000 grid cells per core. For the oblique wave cases LC4.2–LC4.5, each case was simulated using 128 cores, with a computation time of approximately 14 days 10 h.

Table 10
Mean values of mooring tension (kN).

Mooring line	LC.4.1, Wave Dir. = 0°	LC.4.2, Wave Dir. = 15°	LC.4.3, Wave Dir. = 30°	LC.4.4, Wave Dir. = 45°	LC.4.5, Wave Dir. = 60°
ML #1	920.647	927.109	925.797	925.010	918.773
ML #2	1674.611	1650.106	1642.457	1627.089	1598.374
ML #3	914.266	918.127	924.448	933.240	952.762

3.5. Boundary conditions

Combined with the boundary definitions in Figs. 8 and 9, the boundary conditions (B.C.s) for the dynamic pressure, velocity and volume fraction of different cases are listed in Table 5. In the boundaries of which using waveVelocity and waveAlpha B.C.s, the wave-type of Inlet and Front boundaries is 2nd-order Stokes regular wave for wind-wave generation, while the wave-type of Outlet, Back, Inlet-Corner and Outlet-Corner boundaries is the potential current for absorption.

4. Validations for FOWT-UALM-SJTU solver

4.1. UALM calibration

Cases LC.1.1–LC.1.3 evaluate the optimal UALM projection width factor ε ($\varepsilon = 4.0, 4.2, 4.4$) within a uniform grid size of (3.0 m, 3.0 m, 3.0 m). Simulations are performed under steady conditions with 11.4 m/s inflow wind speed, 0° blade pitch angle θ, and 12.1 rpm rotational speed $|\boldsymbol{\Omega}|$, neglecting control actions and blade deformations. For comparation, both the AeroDyn-v14 and AeroDyn-v15 modules within OpenFAST are employed under identical operational conditions. Fig. 11 presents the comparative results, and Table 6 summarizes the mean values and relative differences (Diff.). The results indicate that even between different versions of AeroDyn, the numerical outcomes can't be same. When $\varepsilon = 4.2$, the mean value of rotor power aligns more closely with AeroDyn-v14, which is also the version used for NREL-5MW wind turbine design (Jonkman et al., 2009), while they would be slightly higher than those predicted by AeroDyn-v15. In contrast, the rotor thrust is marginally lower than both versions, but the difference is a little smaller only −3.81%. The gravitational forces are considered as described in Section 2.5.

4.2. Aerodynamic validation

Cases LC.1.4–LC.1.27 are steady aerodynamic validations with $\varepsilon = 4.2$. Different from the former three cases, the control system is turned on, allowing automatic adjustment of rotor speed and blade pitch angle according to five-zone torque control strategy and PID pitch controller. The results are compared with NREL data using FAST with AeroDyn-v14 proposed by Jonkman et al. (2009) and OpenFAST with AeroDyn-v15, as shown in Fig. 12. It can be seen that after control adjustment, FOWT-UALM-SJTU basically matches well with FAST and OpenFAST, especially in high-speed range above 12 m/s. While, in the low-speed range of 3–8 m/s, the rotor power and rotor speed are slightly higher. And near the rated wind speed, the rotor thrust is slightly lower.

Case LC.2 is unsteady aerodynamic validation under a prescribed surge motion defined by the sinusoidal function $x = 8\sin(0.246t)$ under 11 m/s uniform wind speed. The aerodynamic performances are illustrated in Fig. 13, which have undergone phase adjustment. Notably, the results from Cheng et al. (2019) is obtained using an earlier version of FOWT-UALM-SJTU solver. The mean value of power coefficient (C_P) and thrust coefficient (C_T) align closely with reference data, and the C_P amplitude also exhibits strong consistency. However, the C_T amplitude is slightly lower than that in other studies. This discrepancy may stem from the use of a non-open domain with a free surface in the present simulation. Despite this minor deviation, the results confirm the validity of current UALM module for further investigations.

The coefficient C_P and C_T can be expressed as,

$$C_P = \frac{2P}{\rho V^3 A} \tag{18}$$

$$C_T = \frac{2T}{\rho V^2 A} \tag{19}$$

Table 11
Maximum, minimum, STD and mean value of aerodynamic responses.

(a) Rotor power (MW)

Case	Max	Min	STD	Mean
LC.4.1, Wave Dir. = 0°	5.501	4.688	0.237	5.081
LC.4.2, Wave Dir. = 15°	5.515	4.677	0.249	5.083
LC.4.3, Wave Dir. = 30°	5.538	4.609	0.275	5.087
LC.4.4, Wave Dir. = 45°	5.496	4.612	0.266	5.090
LC.4.5, Wave Dir. = 60°	5.446	4.623	0.237	5.083

(b) Rotor thrust (kN)

Case	Max	Min	STD	Mean
LC.4.1, Wave Dir. = 0°	851.133	820.926	6.964	837.272
LC.4.2, Wave Dir. = 15°	848.829	825.787	4.462	838.323
LC.4.3, Wave Dir. = 30°	844.371	828.161	2.944	838.235
LC.4.4, Wave Dir. = 45°	848.097	822.777	5.574	837.575
LC.4.5, Wave Dir. = 60°	856.637	815.784	10.369	838.275

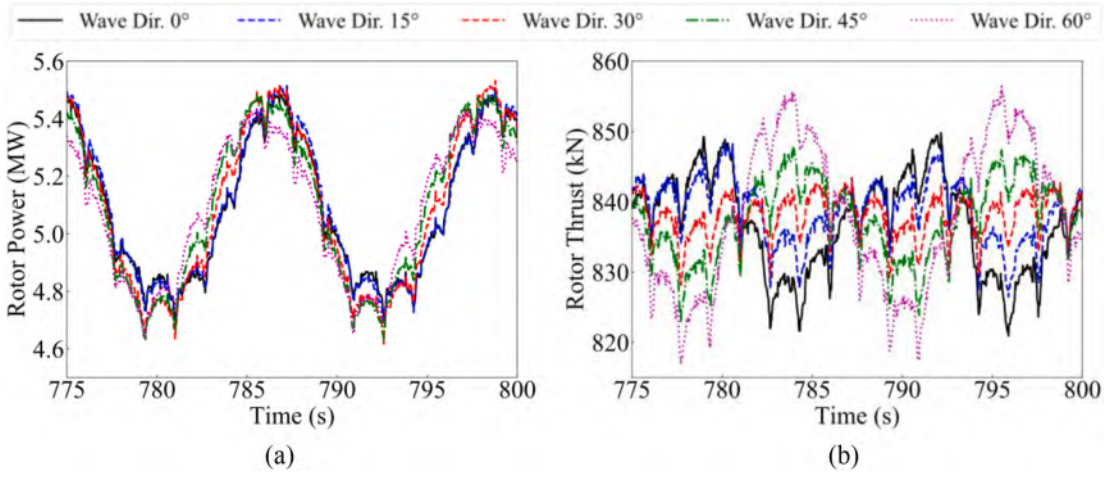

Fig. 22. Aerodynamic responses: (a) rotor power; (b) rotor thrust.

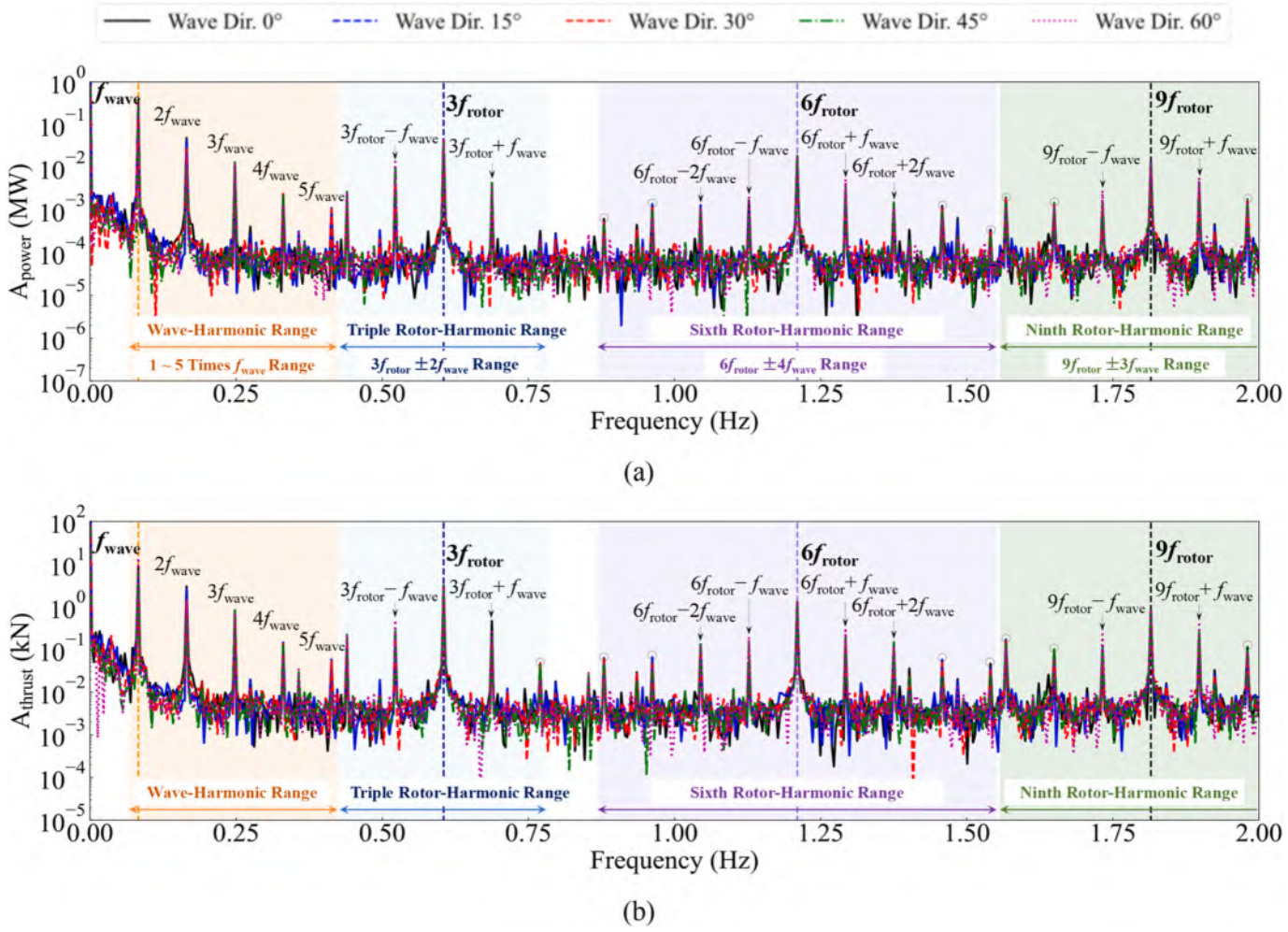

Fig. 23. Amplitude of aerodynamic response under FFT analysis: (a) rotor power; (b) rotor thrust.

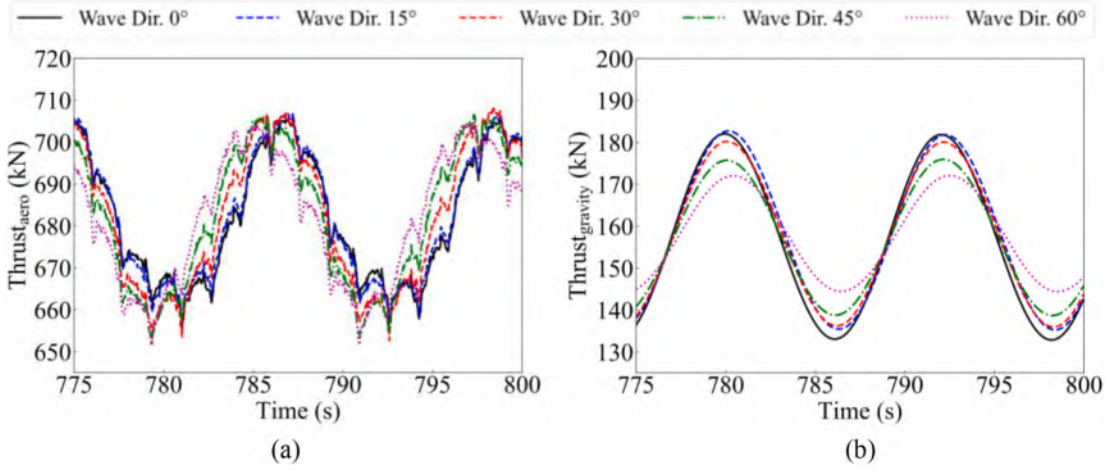

Fig. 24. Comparison of two components in rotor thrust: (a) aerodynamic component; (b) gravitational component.

where, P and T are the rotor power and thrust, respectively; ρ is the air density; V is the wind velocity; A is the rotor area; R is the rotor radius.

4.3. Hydrodynamic validation

In LC.3.1–LC.3.3 cases, grid convergence analysis is conducted under 2nd regular wave condition with $H = 7.58$ m, $T = 12.1$ s. The mesh distribution of these three cases has been listed in Table 4, with grid number of 2,704,011, 5,337,890, 9,547,440, respectively. 3DoF (surge, heave and pitch) motion responses with different grid sizes are presented in Fig. 14. It can be clearly seen from the figure that the LC.3.2 case with medium grid meets the calculation accuracy requirements, which is close to the results of the fine grid (LC.3.3 case). Table 7 and

Table 12
Mean and STD value of each component.

Case	Mean (kN)			STD (kN)		
	Thrust	$\text{Thrust}_{\text{areo}}$	$\text{Thrust}_{\text{gravity}}$	Thrust	$\text{Thrust}_{\text{areo}}$	$\text{Thrust}_{\text{gravity}}$
LC.4.1, 0°	837.272	681.071	157.989	6.964	14.389	17.383
LC.4.2, 15°	838.323	681.226	158.689	4.462	15.002	16.561
LC.4.3, 30°	838.235	681.513	158.309	2.944	16.650	15.581
LC.4.4, 45°	837.575	681.881	157.348	5.574	16.475	13.141
LC.4.5, 60°	838.275	681.508	158.370	10.369	15.423	9.821

Fig. 15 further compare the peak-to-peak amplitude (P2P Amp.) and Response Amplitude Operator (RAO) of 3DoF motion and mooring tension responses at medium grid (LC.3.2 Case) with OpenFAST and other published results. Compared to OpenFAST, the difference in P2P Amp. or RAO of surge, heave, pitch motion, tension of Mooring Line (ML) #1 and ML #2 are 8.19%, −5.79%, 0.389%, 26.38% and 13.65%, respectively. Although discrepancies remain in surge and mooring tensions, the overall agreement with established results is satisfactory, compared to other simulations in Fig. 15. Particularly in the mooring tension, the results are closer to the experiment due to the adoption of the more accurate LMM method, with reference to the mooring line hydrodynamic coefficients from OpenFAST and MoorDyn (mentioned in Section 3.1).

4.4. Fully coupled validation

Conduct fully coupled validation in LC.4.1 case under the condition of 2nd regular wave with $H = 7.58$ m, $T = 12.1$ s, and shear wind profile with 11.4 m/s at hub height ($z = 90$ m). The dynamic response curves are shown in Fig. 16 (phase-adjusted), with the P2P Amp. and average values are summarized in Table 8. The OpenFAST case is from official tutorial, which use AeroDynv15 for aerodynamic calculation. Excellent agreement is observed in hydrodynamic responses, outperforming other numerical studies. Compared with OpenFAST, the differences in P2P Amp. of surge, heave, pitch and ML #2 tension are 4.36%, −4.56%, 2.06%, −4.25%. And the differences in average are −0.60%, −0.037m, −3.31%, 2.27%. For the aerodynamic responses, the average of rotor power and thrust show acceptable errors, which is only 3.13% and −2.20%, respectively.

The remaining discrepancies may be attributed to the CFD method's consideration of fluid viscosity or differences in the numerical coupling framework. Besides, the wind and wave generation modules of new modified waves2Foam (Sections 2.3 and 2.4) are also validated in this case. Extract the wind speed along the vertical line at $x = -150$, $y = 0$ m of the flow field, and perform time-averaged, which matches well with the target exponential shear wind profile, as shown in Fig. 17 (a). And the wave elevation at the same location agrees closely with the Stokes 2nd-order wave theory, as illustrated Fig. 17 (b).

In summary, FOWT is a highly complex system requiring the consideration of numerous coupled factors whose numerical predictions often vary across calculation methods or tools. Nonetheless, the numerical results generated by the present FOWT-UALM-SJTU CFD solver demonstrate acceptable agreement and reliability. These outcomes provide a credible foundation for subsequent research and engineering applications.

5. Results and discussions

5.1. Hydrodynamic motion responses

To obtain stable hydrodynamic and aerodynamic results, a simulation duration of 800 s is adopted in this study. The selection of 0°, 15°, 30°, 45°, 60° five wave directions is motivated by two primary reasons. First, owing to the structural symmetry of OC4 platform, simulations within the 60° range are sufficient to represent the full directional characteristics. Second, since the wind direction remains fixed at 0°, larger wind-wave misalignment angles would be physically unrealistic. In conventional studies with the 0° wave direction, attention is often focused on surge, heave, pitch, and ML #2 tension, while other components are generally neglected due to their minor magnitudes. However, under the oblique wave conditions or wind-wave misalignment, the responses across all 6DoF motions and mooring tensions exhibit distinct behaviours that warrant comparative analysis.

The entire simulation time of the hydrodynamic motion responses is presented in Fig. A.1 (Appendix A), and Fig. 18 provides a more detail display of curves during the last five wave periods, respectively. Notably, except for heave motion which shows minor variations, the other motions undergo significant changes under oblique waves. As the wave direction increases, the equilibrium position of surge motion and amplitude decrease; similarly, the amplitude of pitch motion also decreases. In contrast, sway and roll motions which remain nearly zero under 0° wave condition exhibit pronounced wave-frequency oscillations under oblique excitation. For the yaw motion, as shown in Fig. A.1 (f) and Fig. 18 (f), it displays considerable wave-frequency oscillations at directions of 15°, 30°, and 45°, while the 60° case induces more dominant low-frequency resonant motion. Owing to the symmetric configuration of the OC4 platform, wave loads at 60° produce smaller moment arms relative to the C.M., which may also explain the more pronounced yaw motion observed under 30° wave.

Data from 497.5 s to 800 s (equivalent to 25 wave periods) are extracted for statistical analysis. The maximum, minimum, mean, and standard deviation (STD) of platform motion responses are computed and visualized in the polar coordinate plot as shown in Fig. 19, with mean values summarized in Table 9. These results clearly illustrate the steady-state variation patterns of the platform motions. As wave direction increases, the variation ranges (max-min and STD) of surge and pitch motions gradually decrease. Conversely, the variations of sway and roll motions exhibit a growing trend. While, yaw motion shows a trend of initial increase followed by decrease. These variation characteristics are closely related to the structural and mooring system symmetry of OC4 platform. Significant changes in mean values (equilibrium positions) are observed particularly in surge and sway motions. As the wave direction shifts, the mean values of surge motion decrease by 3.52%, 4.62%, 6.98%, 11.70% at four oblique wave directions, compared to 0°. Meanwhile, motion response amplitude analysis based on Fast Fourier Transform (FFT) is provided in Appendix B.1.

5.2. Mooring tension analysis

Regarding mooring tensions, surge motion induced by 0° wind still dominates the platform motion in *xoy*-plane, so the ML #2 consistently exhibits the highest tension among the three lines as shown in Fig. 20. Although the mooring tensions of ML #1 and ML #3 increase with wave direction, this increase is not symmetric: the mooring tension of ML #1 rises much more significantly than in ML #3. Particularly when the wave direction at 60°, the difference in amplitude of ML #1 and ML #3 increase becomes pronounced, as shown in Fig. 20 (a) and (c). From the kinematic perspective, ML #2 bears a greater share of the load that would otherwise act on ML #3.

Performing the same operation as hydrodynamic motion responses,

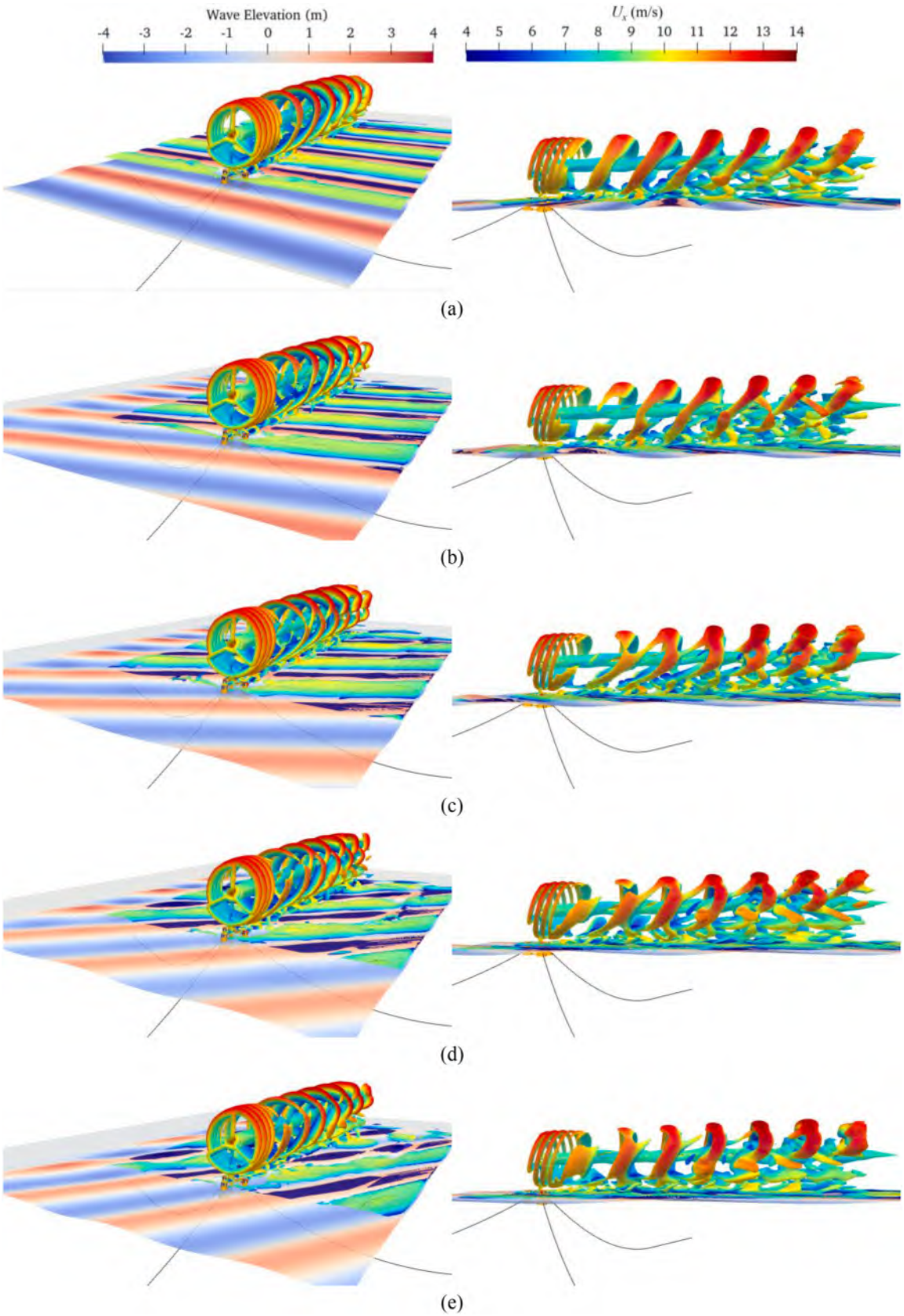

Fig. 25. FOWT wake vortex at the last time (Q = 0.005): (a) Case LC.4.1 at 0° wave direction; (b) Case LC.4.2 at 15° wave direction; (c) Case LC.4.3 at 30° wave direction; (d) Case LC.4.4 at 45° wave direction; (e) Case LC.4.5 at 60° wave direction.

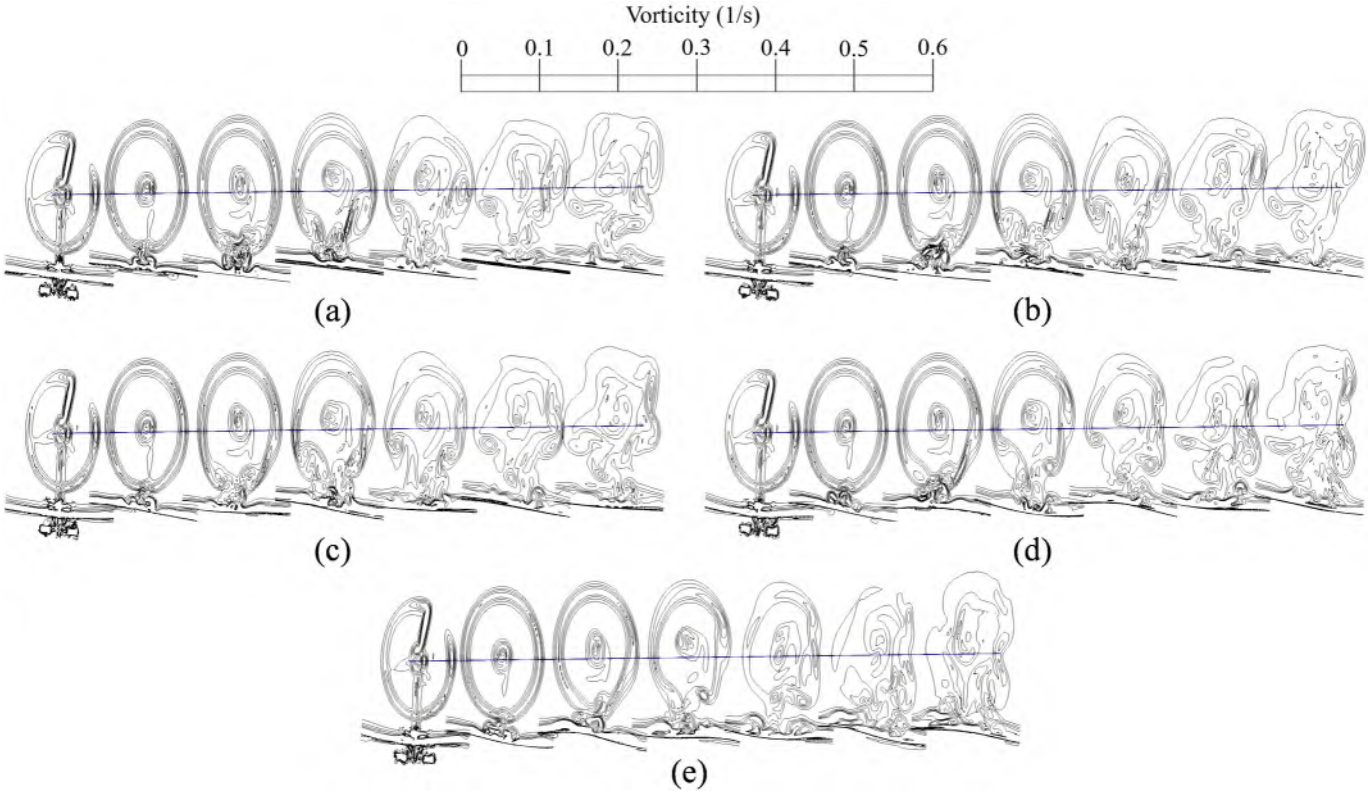

Fig. 26. FOWT wake vorticity iso-surfaces extracted downstream at the last time: (a) Case LC.4.1 at 0° wave direction; (b) Case LC.4.2 at 15° wave direction; (c) Case LC.4.3 at 30° wave direction; (d) Case LC.4.4 at 45° wave direction; (e) Case LC.4.5 at 60° wave direction.

the max-minimum value region, mean value and STD region are illustrated in Fig. 21, and the mean values are listed in Table 10. As the wave direction shifts, the mean value of ML #2 and ML #3 tensions gradually decrease. Specifically, at 60°, these values decrease by 4.55%, and 2.08%, compared to those at 0°. In contrast, the ML #1 tension remains relatively unchanged. Meanwhile, the amplitudes of each line based on FFT analysis are provided in Appendix B.2.

5.3. Aerodynamic responses

The stabilized aerodynamic response (Fig. 22, Table 11) reveals minimal change (<1%) in the mean values of both rotor power and thrust. However, their fluctuation patterns differ significantly. While power fluctuations remain negligible, thrust fluctuation exhibits a non-monotonic trend with wave direction, minimizing at 30°. Specifically, the STD value of thrust decreases by 57.73% to 2.944 kN at 30° (from 6.964 kN at 0°), before increasing by 48.89% to 10.369 kN at 60°. Despite these substantial oscillations, the mean thrust remains largely unaffected.

The aerodynamic response was further characterized using FFT analysis on the data from 497.5 s to 800 s, with the amplitude-frequency spectrum presented in Fig. 23 (logarithmic vertical axis). The spectrum is divided into distinct frequency intervals: the wave-harmonic range, the third rotor-harmonic range (3frotor), and higher rotor-harmonics. A quantitative analysis of the amplitudes within each interval is elaborated in detail in *Appendix. B.3*.

5.4. Gravitational effects on rotor thrust

As mentioned in Section 2.5, the rotor thrust represents the force along shaft direction, which comprises both aerodynamic and gravitational components. It could not purely reflect the aerodynamic behaviours, explaining the divergent trends between rotor power and thrust in Fig. 22. The separation of these two components in Fig. 24 reveals that the oscillation trend of the aerodynamic component mirrors the power response pattern in Fig. 22 (a), showing relatively stronger fluctuations at 30° wave direction. Comparative analysis with Fig. 18 (e) indicates an inverse phase relationship between aerodynamic responses and platform pitch motion. When the pitch angle approaches its trough (around 0°), the aerodynamic responses reach their peaks. Regarding the gravitational component, an increase in pitch motion alters the orientation of the shaft, thereby increasing the contribution of gravity to the thrust. As a result, the variation in Fig. 24 (b) exhibits the same trend as the pitch motion. It is precisely due to this phase difference that the superposition of the components in Fig. 24 (a) and (b) causes the peaks of rotor thrust in Fig. 22 (b) to occur between the peaks and troughs of the pitch motion, rather than aligning with it. This anomalous variation pattern, which is driven by gravitational effects, requires particular attention.

Further statistical analysis of the curves in Fig. 24 was conducted and the results are summarized in Table 12. In terms of mean values, the gravitational component contributes approximately 18% to the total rotor thrust, indicating that neglecting gravity would lead to a significant underestimation of thrust magnitude. From the perspective of STD, it can also be observed that due to the inverse-phase relationship between the two components over time, the fluctuation of the gravitational component dominates at wave directions of 0° and 15°, while the aerodynamic component dominates at 45° and 60°. At 30°, both components contribute comparably, resulting in a more moderate variation in total rotor thrust under this wave direction.

5.5. Turbine wake analysis

The key advantage of the CFD approach lies in its capacity for high-fidelity flow field analysis. Fig. 25 visualizes the wave surface and wake vortices at $t = 800$s. In order to better display wave elevation, the vortex structure near the free surface at front in the figure has been cut. The free

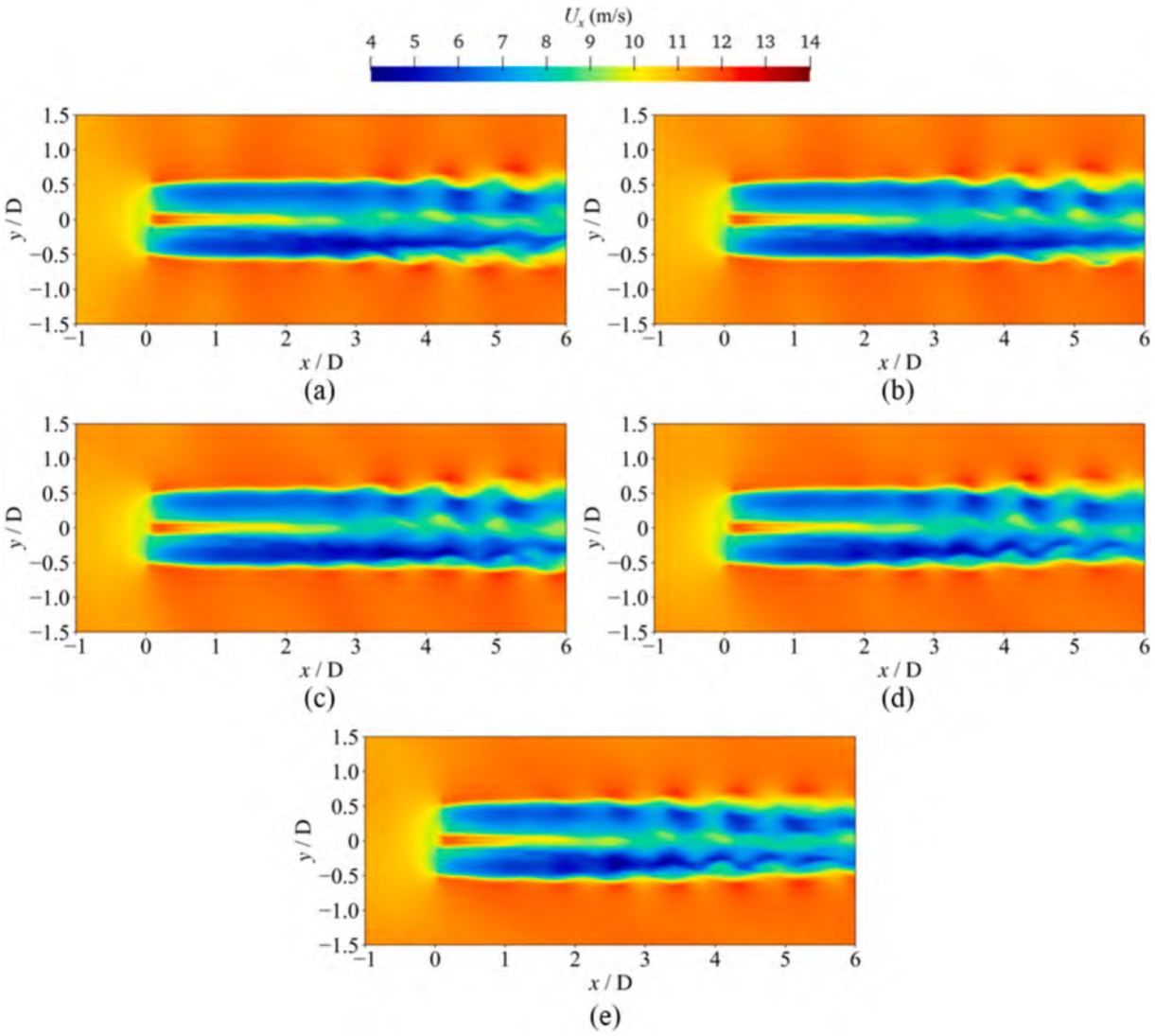

Fig. 27. Wake velocity parallel *xoy*-plane at $z = 90$ m (hub height) at the last time: (a) Case LC.4.1 at 0° wave direction; (b) Case LC.4.2 at 15° wave direction; (c) Case LC.4.3 at 30° wave direction; (d) Case LC.4.4 at 45° wave direction; (e) Case LC.4.5 at 60° wave direction.

surface is rendered by wave elevation, and the vortex structures are extracted based on the Q-criterion ($Q = 0.003\ s^{-2}$) and colored by the velocity U_x. The figure reveals three key processes: (1) the rotating turbine blades generate distinct vortex patterns: annular tip vortices shed from the blade tips and helical root vortices originating near the hub; (2) The annular tip vortices will independently develop 3–4 annular structures downstream and then begin merging into a larger vortex ring structure; (3) The vortices generated from the platform's upper surface and side walls, as well as those introduced by wave motion, altering the turbine wake vortices. And under oblique waves, the far-wake vortex rings become disorganized near the free surface. Vorticity iso-surfaces in Fig. 26 further illustrate that the coherent vortex structures break into smaller fragments under oblique waves, especially at 45° and 60°. This phenomenon stems from the coupling between the shear wind profile and wave elevation, as described by Eq. (10). Although the mean wind is aligned with the x-direction, its interaction with directionally varying waves produces peak-trough patterns aligned with the wave direction.

Fig. 27 presents the wake velocity in a horizontal plane parallel to *xoy*-plane at hub height ($z = 90$ m). Two characteristic wake development phenomena are observed: wake meandering and interface mixing. In the low-velocity zone (blue region), with increasing wave direction, the lower wake (negative *y*-axis direction) exhibits pronounced meandering, while the upper wake (positive y-axis direction) shows intermittent breakup. Regarding the interface mixing, the mid-speed wake region (yellow and green regions), which has already begun to mix with the outer flow under at 0° wave direction, appears more consolidated under oblique waves. Fig. 28 further illustrates the vorticity magnitude on the same plane. It is clearly visible that the wake vortices also exhibit enhanced meandering with increasing wave direction. Additionally, based on the color intensity, although the low-speed wake region under the 0° condition does not display meandering, it contains multiple vortical structures with higher intensity that likely promote mid-speed wake boundary diffusion. We hypothesize that the observed wake meandering may be primarily driven by increased sway and roll motions induced by oblique waves. While, the reduced surge and pitch motions coupled with the modified inflow field under skewed wave directions likely contributes to an overall decrease in vorticity within the wake, resulting in a more consolidated wake region.

5.6. Turbine wake velocity deficit

To further evaluate the impact of wake meandering and wake interface mixing under different wave directions, the time-averaged wake velocity $U_{\mathrm{mean},x}$ is computed using data sampled every 0.5 s

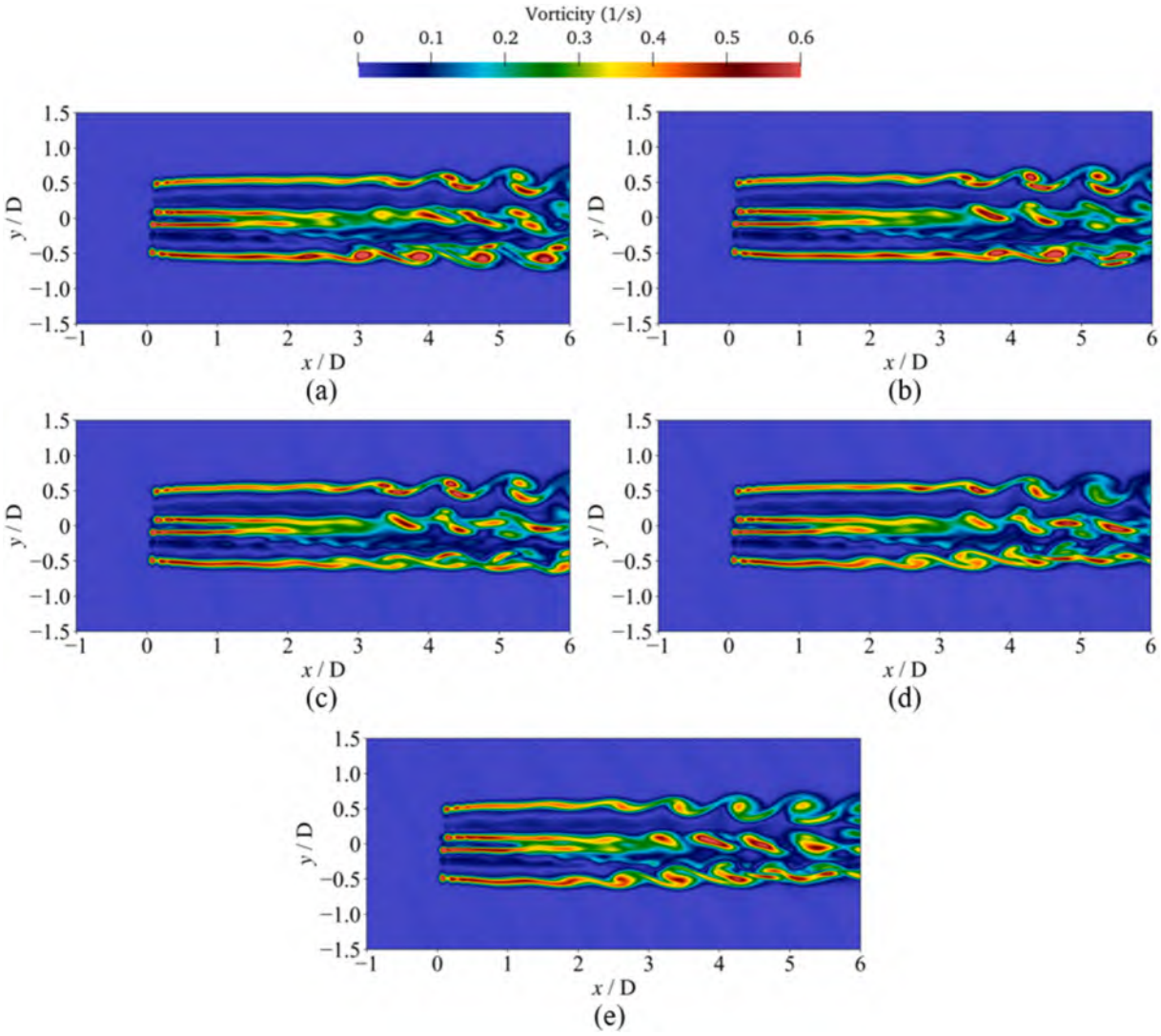

Fig. 28. Wake vorticity parallel *xoy*-plane at $z = 90$ m (hub height) at the last time: (a) Case LC.4.1 at 0° wave direction; (b) Case LC.4.2 at 15° wave direction; (c) Case LC.4.3 at 30° wave direction; (d) Case LC.4.4 at 45° wave direction; (e) Case LC.4.5 at 60° wave direction.

from 497.5 s to 800 s. Fig. 29 shows the $U_{\mathrm{mean},x}$ on the horizontal plane, where D = 126 m represents the rotor diameter. Velocity deficit curves are extracted at downstream distances from 1D to 6D, as illustrated in Fig. 30. Here, $U_{\mathrm{wind}} = 11.4$ m/s and the velocity deficit $\Delta u = U_{\mathrm{wind}} - U_{\mathrm{mean,x}}$. A larger Δu corresponds to greater velocity loss. At 30° wave direction, although the wake region contracts between 2D and 4D, it experiences an extreme evident from 5D to 6D due to the combined effects of wake development and external wave-induced disturbances, resulting in a significantly larger velocity deficit compared to other cases. According to the insights from the vorticity analysis in Fig. 28 (c), the power output in Fig. 22 (a), and the yaw motion response in Fig. 18 (f), we conclude that although noticeable wake meandering occurs at 30°driven primarily by sway and roll motions, the overall vortex structure remains relatively coherent downstream. Furthermore, combined with negative yaw motion and stronger power fluctuations, this enhances rotor energy extraction and enlarges the wake deficit. In contrast, wake contraction is more evident at 45° and 60° wave directions. However, the maximum velocity deficit at the wake centre and across the entire region, remain similar among all conditions.

A single-plane analysis is insufficient to fully characterize wake behavior, particularly under non-turbulent inflow. Therefore, we extract flow data at multiple downstream cross-sections (3D–6D), as visualized in Fig. 31. To quantitatively assess wake recovery, the Available Power (AP) coefficient is computed for a hypothetical downstream rotor (Vollmer et al., 2016; Wei et al., 2021; Giri Ajay and Simao Ferreira, 2024), defined as,

$$C_{AP} = \frac{\iint_S 0.5\rho\bar{u}^3 dydz}{\iint_S 0.5\rho u^3(z) dydz} \tag{20}$$

where, $\bar{u}$ denotes the time-averaged wake velocity $U_{\mathrm{mean},x}$, $u(z)$ is the shear wind velocity, and S represents the rotor area.

The resulting C_{AP} values are summarized in Table 13, which demonstrate that beyond 4D downstream, C_{AP} under oblique waves are consistently higher than that under the 0° condition. Among all directions, the 45° wave yields the most favorable recovery performance.

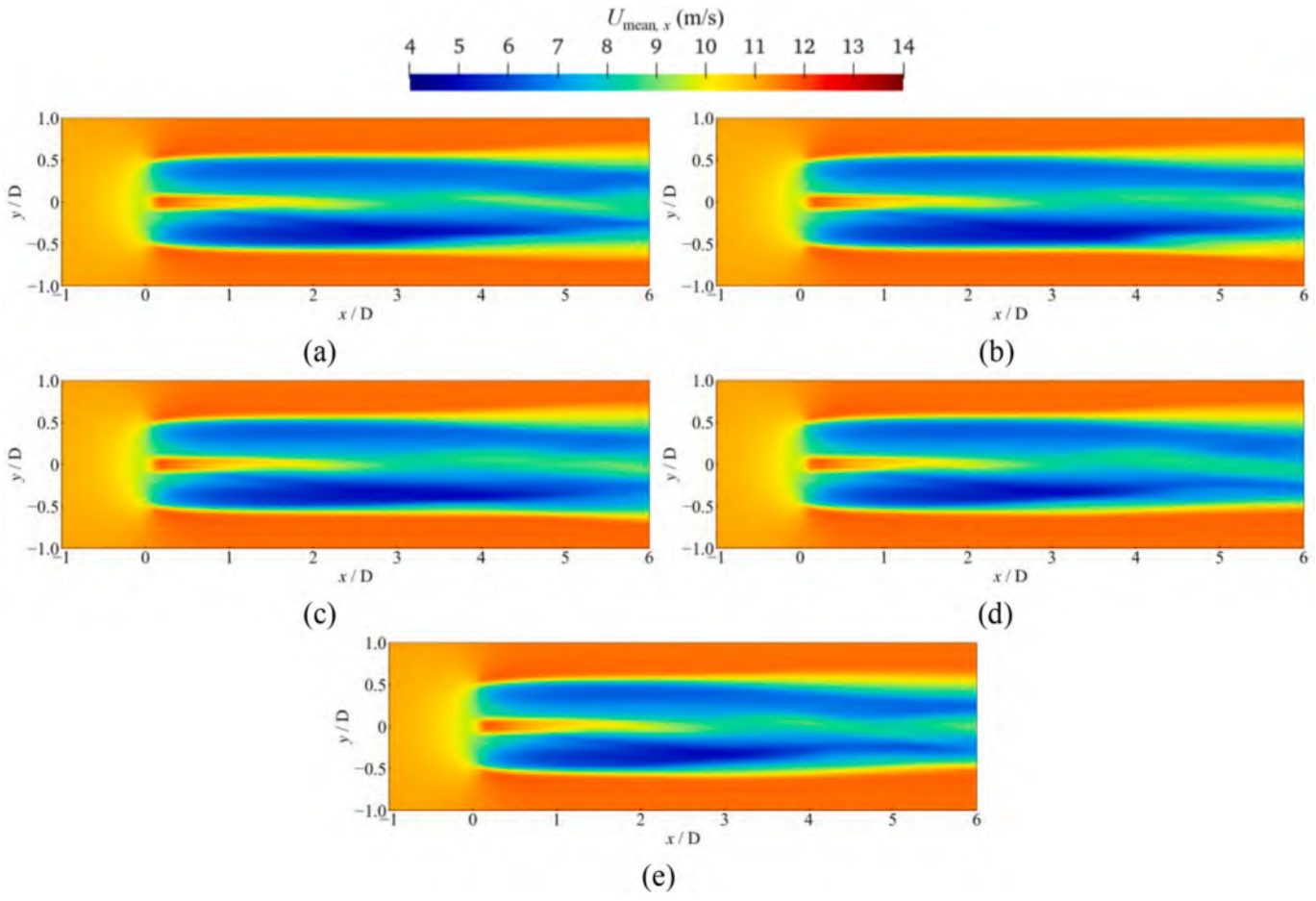

Fig. 29. Time-average wake vorticity parallel *xoy*-plane at $z = 90$ m (hub height): (a) Case LC.4.1 at 0° wave direction; (b) Case LC.4.2 at 15° wave direction; (c) Case LC.4.3 at 30° wave direction; (d) Case LC.4.4 at 45° wave direction; (e) Case LC.4.5 at 60° wave direction.

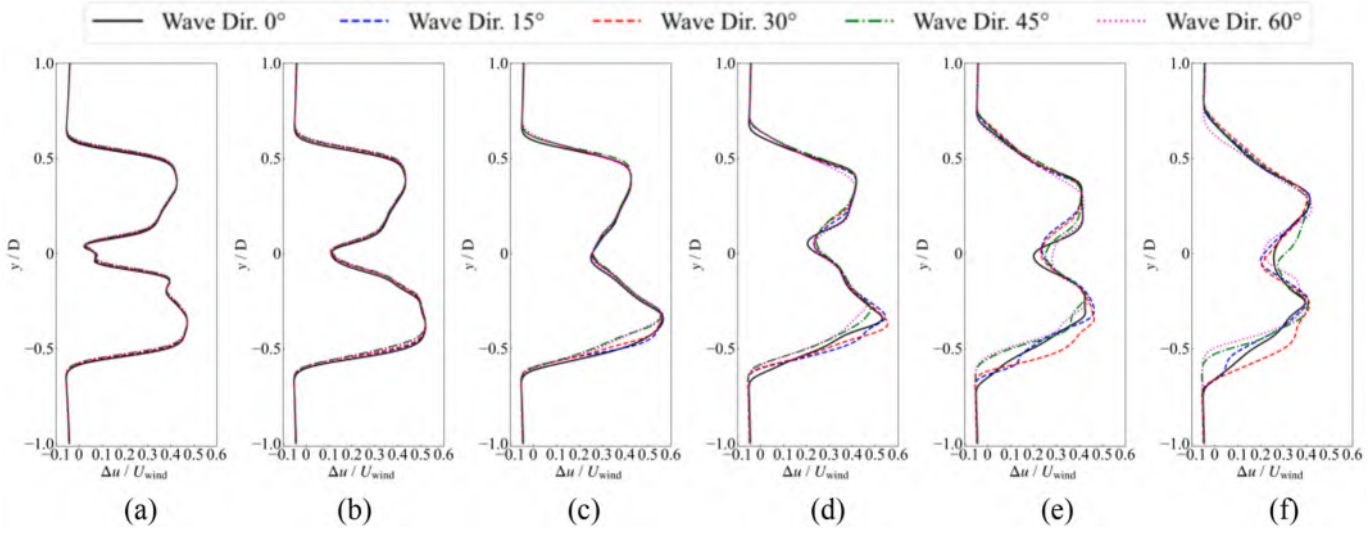

Fig. 30. Wake vorticity deficit profile paralle *xoy*-plane at hub height: (a) $x = 1.0$ D; (b) $x = 2.0$ D; (c) $x = 3.0$ D; (d) $x = 4.0$ D; (e) $x = 5.0$ D; (f) $x = 6.0$ D.

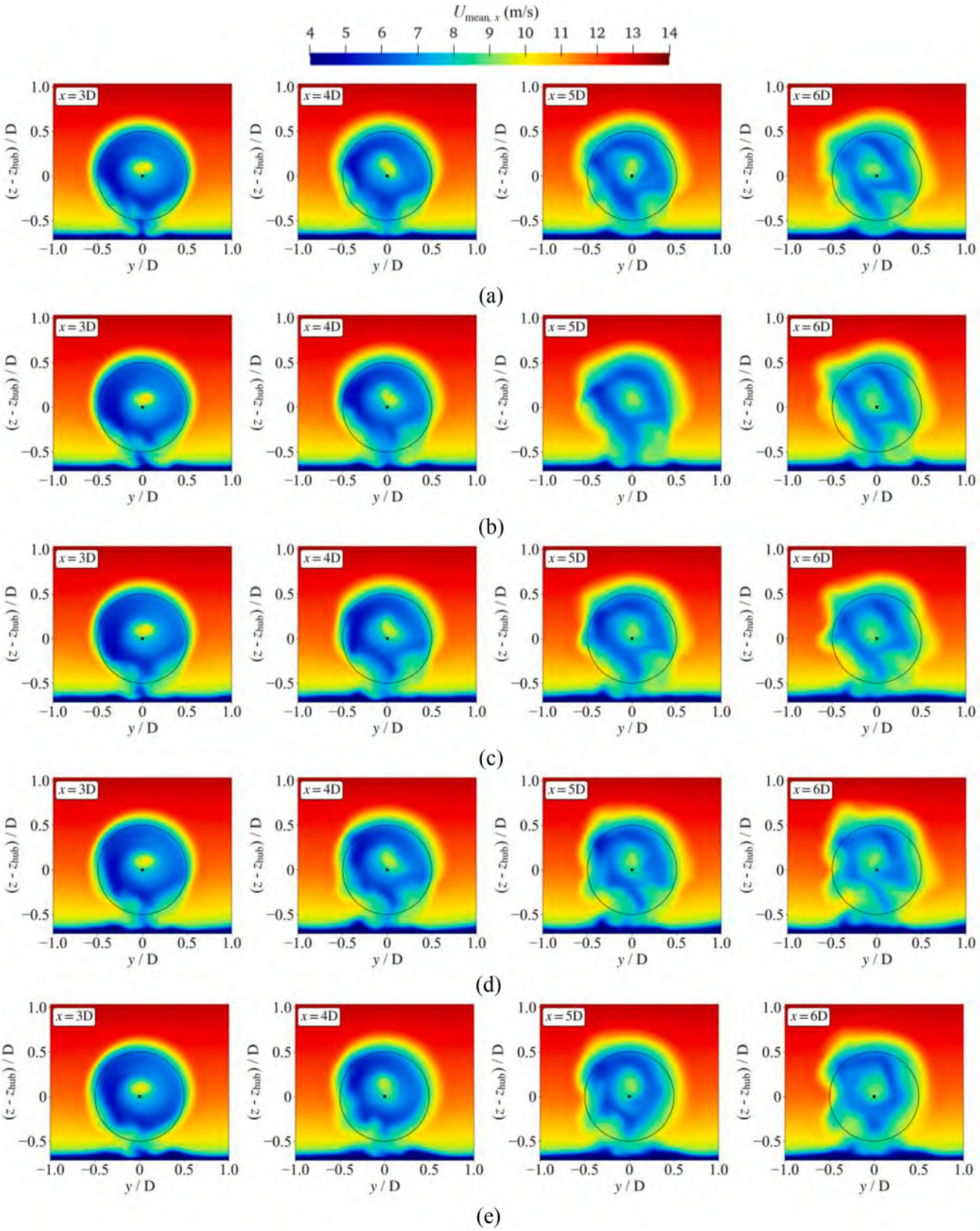

Fig. 31. Wake velocity at multiple downstream cross-sections: (a) Case LC.4.1 at 0° wave direction; (b) Case LC.4.2 at 15° wave direction; (c) Case LC.4.3 at 30° wave direction; (d) Case LC.4.4 at 45° wave direction; (e) Case LC.4.5 at 60° wave direction.

Table 13
Normalized available power (C_{AP}).

Case	3D	4D	5D	6D
LC.4.1, Wave Dir. = 0°	0.2311	0.2565	0.2904	0.3232
LC.4.2, Wave Dir. = 15°	0.2320	0.2611	0.3021	0.3387
LC.4.3, Wave Dir. = 30°	0.2344	0.2612	0.3003	0.3412
LC.4.4, Wave Dir. = 45°	0.2387	0.2665	0.3012	0.3389
LC.4.5, Wave Dir. = 60°	0.2372	0.2661	0.3004	0.3312

Compared to the 3D downstream plane, the C_{AP} increases by 11.65%, 26.18%, and 41.98% at the 4D–6D planes, respectively. These results indicate a progressive acceleration of wake recovery with increasing downstream distance, which enhances the wind energy capture potential of downstream turbines. This finding provides valuable guidance for the layout design of floating wind farms. Furthermore, combined with the observation in Fig. 26 that the wake vortex structure under the 45° condition appears more fragmented, we reasonably hypothesize that this improvement is primarily attributable to the influence of wave direction on the shear wind profile, which introduces stronger perturbations in the wake region.

6. Conclusions

Based on OpenFOAM, this study extends the open-source tool waves2Foam to support shear wind making by relaxation zone method, and couples it with FOWT-UALM-SJTU solver to achieve fully coupled simulations of the NREL-5MW OC4 semi-submersible FOWT. Additionally, the UALM is enhanced by incorporating the gravitational forces of the blades and hub into the rotor thrust calculation. The solver is rigorously validated through aerodynamic predictions, hydrodynamic calculation, and fully coupled simulation, demonstrating good agreement with experimental and numerical results. Based on this, conduct numerical simulations under misaligned wind-wave conditions (oblique waves), investigating the hydrodynamic, aerodynamic, and wake characteristics. The main conclusions include:

(1) In five (0°, 15°, 30°, 45°, 60°) wind-wave misalignment conditions, the hydrodynamic responses vary significantly, except heave. As the wave direction increases, the equilibrium position and amplitude of surge decrease, as same as the pitch motion. In contrast, sway and roll motions exhibit substantial wave-frequency oscillations under oblique excitation. Besides, due to the symmetrical nature of the platform, the maximum mean value and oscillation of yaw motion occurred at 30°. Mooring line tensions respond differently: ML#2 decreases gradually, ML#1 increases, and ML#3 decreases then increases. Especially at 60°, the tension amplitude of ML #1 becomes comparable to ML #2. Practically, these variations in mooring load distribution highlight the need to incorporate wind-wave misalignment effects into mooring system design margins for enhanced reliability.

(2) Aerodynamic response reveals minimal change (<1%) in the mean values of both rotor power and thrust, while their fluctuation patterns differ significantly. The rotor thrust amplitude first decreases and then increases, reaching a minimum at 30° wave direction, affected by the gravitational forces of blade and hub mass. FFT analysis identifies distinct frequency intervals: the wave-harmonic range, the third rotor-harmonic range, and higher rotor-harmonics ranges. The first wave-harmonic ($f_{\text{wave}} = 0.0826$ Hz) always dominates in wave-frequency range. In the other ranges, each interval is centered on a multiple of third rotor-harmonic, again accompanied by wave-related sidebands.

(3) Visualization based on the Q-criterion reveals that the turbine generates blade tip and root vortices. The annular tip vorticities would independently develop 3–4 circles downstream and then begin to merge into a larger ring vortex structure. Under oblique wave directions, these coherent structures break into fragmented vortices near the free surface due to interactions between directional waves and the shear wind profile, especially at 45° and 60°. Wake analysis at hub height shows increased meandering and intermittent breakup of the low-velocity region under oblique waves. While the mid-velocity boundary mix is most significant in 0°. Quantification of wake recovery using the Available Power method indicates that oblique conditions accelerate recovery, particularly 45°, attributed to stronger flow disturbances and fragmented vortex structures induced by wave direction. From a design perspective, this accelerated wake recovery under 45° oblique waves suggests potential benefits in farm layout optimization through staggered turbine arrangements.

This study establishes a CFD-based framework for simulating misaligned wind-wave conditions, provides comprehensive aerodynamic and hydrodynamic data under oblique seas, offering valuable insights for the design of FOWTs in full-scale conditions. Nevertheless, this study still has some limitations. The investigation is confined to the OC4 semi-submersible FOWT under a single shear wind profile and regular waves with misalignment, without considering turbulent wind or irregular waves, leaving the applicability scope insufficiently validated. Methodologically, the ALM accuracy depends heavily on the projection factor, and widely parametric analysis is lacking. Structural flexibility and rotor control under complex conditions also require attention. The coupling between wake meandering and motion response needs further study. Additionally, we also tried to simulate wind-wave misalignment conditions using OpenFAST, which shows a discrepancy at wave directions of 45° and 60°, pointing to the necessity of deeper investigation into the complex interplay between wave-induced wind fields and turbine aerodynamics.

CRediT authorship contribution statement

Yingjie Xue: Writing – original draft, Validation, Software, Methodology, Investigation, Formal analysis, Conceptualization. **Jinguang Wang:** Writing – review & editing, Validation, Resources, Investigation, Data curation. **Weiwen Zhao:** Writing – review & editing, Supervision, Resources, Formal analysis, Conceptualization. **Decheng Wan:** Writing – review & editing, Supervision, Methodology, Funding acquisition, Conceptualization.

Declaration of competing interest

The authors declare that they have no known competing financial interests or personal relationships that could have appeared to influence the work reported in this paper.

Acknowledgements

This work is supported by the National Natural Science Foundation of China (Grant No. 52131102), the Development and Application Project of Ship CAE Software, and the Research and Application Demonstration Project of Key Technologies for Safeguarding of Container vessels in Ningbo Zhoushan Port Based on Intelligent Navigation (Grant No. ZJHGFW-2024-27), to which the authors are most grateful.

Appendix A. Figure and Table

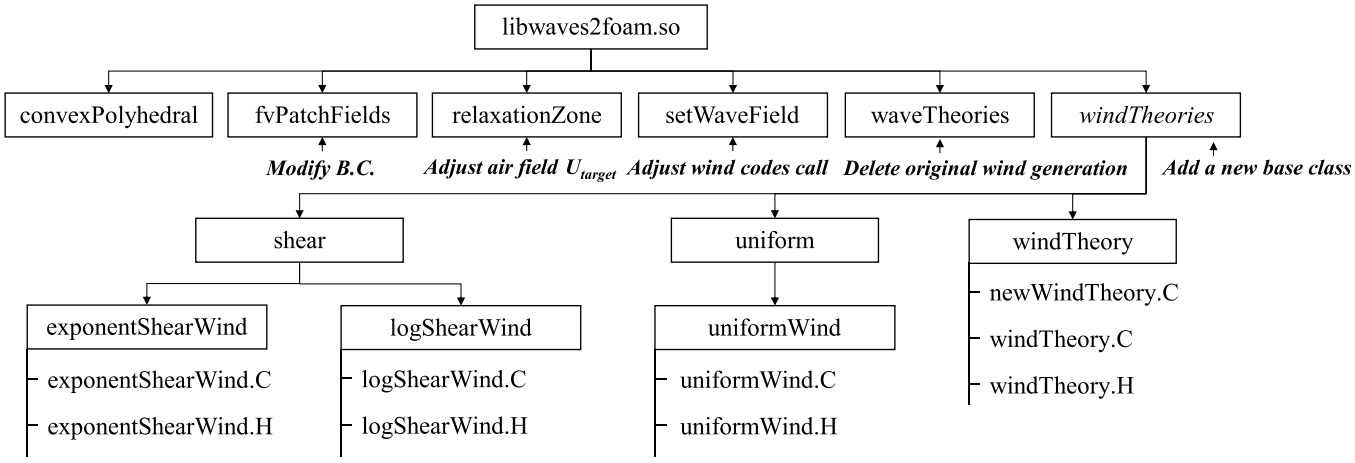

Fig. A.1. File structure of waves2Foam with new added windTheories base class.

Table A.1
OC4 FOWT properties.

(a) NREL-5MW wind turbine with tower	
Properties	Value
Rated wind speed, rated rotor speed	11.4 m/s, 12.1 rpm
Rotor, hub diameter	126 m, 3 m
Hub, tower height	90 m, 87.6 m
Overhang, shaft tilt, precone	5.0191 m, 5°, 2.5°
Distance from yaw bearing to shaft (Twr2Shft)	1.96256 m
Blade mass, hub mass	17,740 kg, 56,780 kg
Nacelle mass, tower mass	240,000 kg, 249,718 kg
Nacelle C.M. to yaw bearing C.M.	(1.9 m, 0, 1.75 m)
Tower C.M. to SWL	43.4 m
(b) OC4 floating platform (with ballast water)	
Properties	Value
Platform mass, including ballast water	1.3473×10^7 kg
Draft	20 m
C.M. location bellow SWL	13.46 m
Platform roll inertia about C.M. (I_{xx})	6.827×10^9 kg m^2
Platform pitch inertia about C.M. (I_{yy})	6.827×10^9 kg m^2
Platform yaw inertia about C.M. (I_{zz})	1.226×10^{10} kg m^2
(c) Three-line mooring system	
Properties	Value
Unstretched length	835.5 m
Anchors radius, fairleads radius	837.6 m, 40.868 m
Mooring line diameter	0.0766 m
Dry mass density, wet mass density	113.35 kg/m, 108.63 kg/m
Young's Modulus (E)	1.6353×10^{11} N/m^2
Extensional stiffness (EA)	7.536×10^8 N

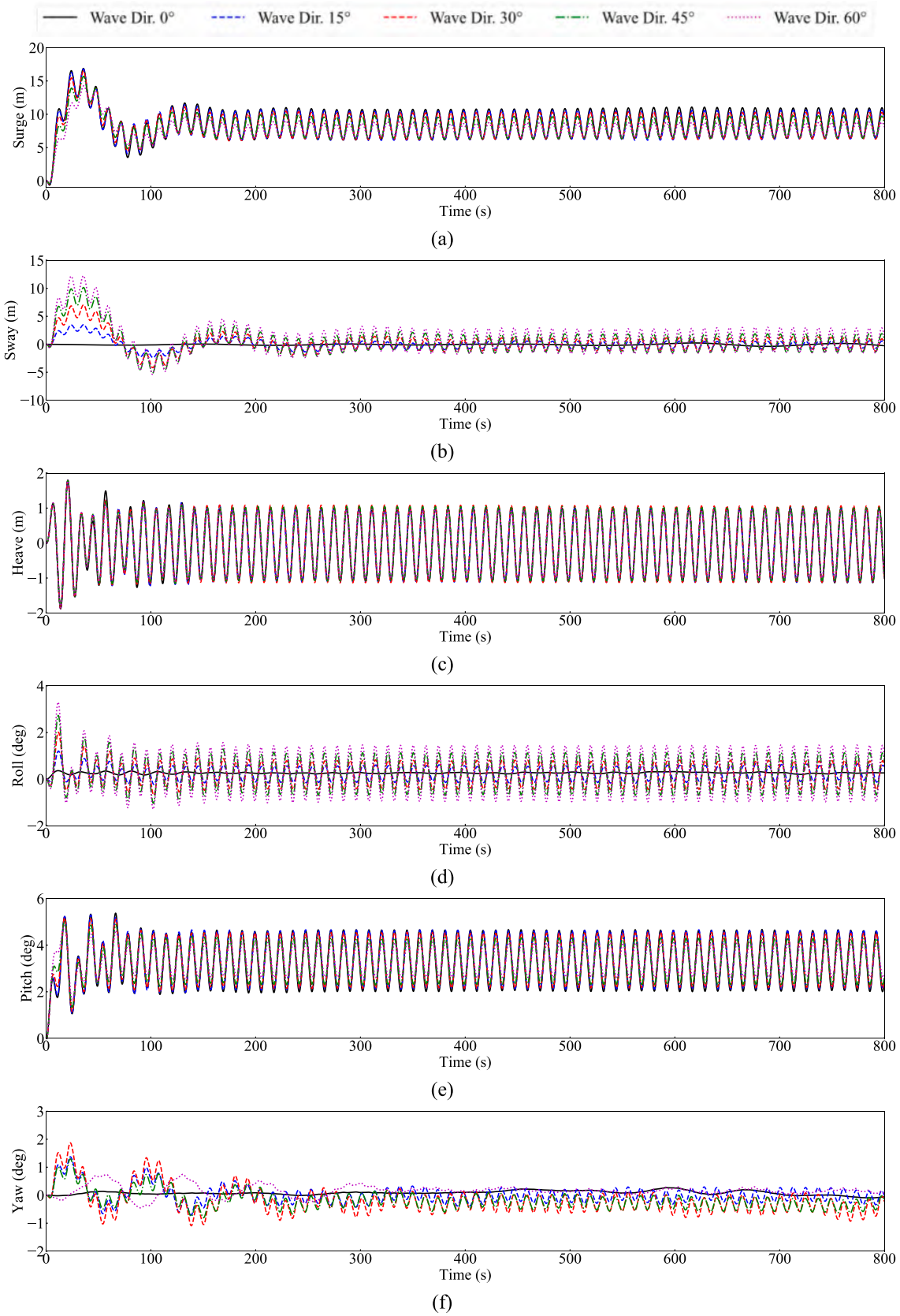

Fig. A.2. 6DoF motion responses in in entire simulation time: (a) surge motion; (b) sway motion; (c) heave motion; (d) roll motion; (e) pitch motion; (f) yaw motion.

Appendix B. FFT Analysis

Appendix B.1 FFT analysis of hydrodynamic motion responses

Fast Fourier Transform (FFT) analysis was conducted over the last 25 wave periods of the hydrodynamic motion responses (Fig. A.1 and Fig. 18), as listed in Table B.1. Both surge and pitch motion amplitudes decrease with wave directions. Similar to STD, the surge motion amplitudes decrease by 4.57%, 12.21%, 27.76%, 52.79%, and the pitch motion amplitudes decrease by 4.67%, 10.41%, 24.50%, 43.57%. While the sway and roll motion amplitude increase from 0 m, 0° to 2.235 m, 1.204°, at 60° wave direction.

Table B.1
Amplitude (under FFT analysis) of hydrodynamic responses.

Hydrodynamic motion responses	LC.4.1, Wave Dir. = 0°	LC.4.2, Wave Dir. = 15°	LC.4.3, Wave Dir. = 30°	LC.4.4, Wave Dir. = 45°	LC.4.5, Wave Dir. = 60°
Surge (m)	2.277	2.173	1.999	1.645	1.075
Sway (m)	0.002	0.645	1.109	1.638	2.235
Heave (m)	1.059	1.065	1.096	1.056	0.976
Roll (deg)	0.003	0.352	0.610	0.906	1.204
Pitch (deg)	1.306	1.245	1.170	0.986	0.737
Yaw (deg)	0.003	0.236	0.326	0.242	0.041

Appendix B.2 FFT analysis of mooring tension

Performing FFT analysis of mooring tension, and the amplitude of each line are listed in Table B.2. As wave direction increases, the amplitude of ML #1 tension gradually increases, while that ML #2 tension decreases, and ML #3 tension shows an initial decrease followed by an increase. Notably, at 60°, the mooring tension amplitudes of these three lines reach 139.260 kN, 140.884 kN, and 74.625 kN, with ML #1 becoming comparable to ML #2.

Table B.2
Amplitude (at wave frequency) of mooring tension.

Mooring tension	LC.4.1, Wave Dir. = 0°	LC.4.2, Wave Dir. = 15°	LC.4.3, Wave Dir. = 30°	LC.4.4, Wave Dir. = 45°	LC.4.5, Wave Dir. = 60°
ML #1 (kN)	55.460	88.571	103.834	112.220	139.260
ML #2 (kN)	493.592	419.836	382.685	306.069	140.884
ML #3 (kN)	55.295	41.739	36.312	39.951	74.625

Appendix B.3 FFT analysis of aerodynamic responses

In the wave-harmonic range of, the first wave-harmonic (f_{wave} = 0.0826 Hz) dominates. As listed in Table B.3, the amplitudes of rotor power and thrust at higher wave-harmonics ($2f_{wave}$, $3f_{wave}$) decrease significantly. For instance, at $2f_{wave}$, rotor power amplitude accounts for approximately 14.92%, 12.90%, 7.03%, 3.69%, and 6.95% of those at f_{wave}, across five wave directions. And, at $3f_{wave}$, these values would drop to approximately 3.69%, 3.04%, 3.15%, 3.55%, and 3.54%. In terms of rotor thrust, the amplitudes at $2f_{wave}$ are 34.60%, 59.44%, 87.50%, 9.02%, and 10.37% of those at f_{wave}, while they decrease to 9.21%, 15.29%, 49.39%, 11.80%, and 5.16% at $3f_{wave}$.

Within the third rotor-harmonic range ($3f_{rotor}$ = 0.2479 Hz, blade-passing frequency), the dominant peak is accompanied by wave-induced sidebands. The absolute amplitude here is governed by wind speed, showing little variation with wave direction. However, from the perspective of proportion, it is different. The amplitudes of rotor power at $3f_{rotor}$ under different wind direction are 13.21%, 12.49%, 11.02%, 11.16%, and 12.56% of those at f_{wave}, while the relative ratios of thrust amplitude vary more significantly, reaching 36.74%, 71.08%, 196.28%, 43.05%, and 21.25%. As for the amplitudes corresponding to the sum and difference frequencies, only a portion can match $3f_{wave}$, while the other amplitudes are relatively small.

Table B.3
Peak amplitude value of aerodynamic responses under FFT analysis.

(a) Rotor power (MW)						
Case	f_{wave}	$2f_{wave}$	$3f_{wave}$	$3f_{rotor}$	$6f_{rotor}$	$9f_{rotor}$
	0.0826 Hz	0.1653 Hz	0.2479 Hz	0.605 Hz	1.210 Hz	1.815 Hz
LC.4.1, Wave Dir. = 0°	0.3277	0.0489	0.0121	0.0433	0.0185	0.013
LC.4.2, Wave Dir. = 15°	0.3450	0.0445	0.0105	0.0431	0.0186	0.0129
LC.4.3, Wave Dir. = 30°	0.3840	0.0270	0.0121	0.0423	0.0184	0.0127
LC.4.4, Wave Dir. = 45°	0.3718	0.0121	0.0132	0.0415	0.0182	0.0125
LC.4.5, Wave Dir. = 60°	0.3305	0.0230	0.0117	0.0415	0.0184	0.0124
(b) Rotor thrust (kN)						
Case	f_{wave}	$2f_{wave}$	$3f_{wave}$	$3f_{rotor}$	$6f_{rotor}$	$9f_{rotor}$
	0.0826 Hz	0.1653 Hz	0.2479 Hz	0.605 Hz	1.210 Hz	1.815 Hz
LC.4.1, Wave Dir. = 0°	8.6165	2.9810	0.7936	3.1660	1.2837	0.8338
LC.4.2, Wave Dir. = 15°	4.4236	2.6294	0.6764	3.1445	1.2798	0.8302
LC.4.3, Wave Dir. = 30°	1.5717	1.3753	0.7763	3.0849	1.2556	0.8118
LC.4.4, Wave Dir. = 45°	7.0120	0.6327	0.8272	3.0192	1.2582	0.8175
LC.4.5, Wave Dir. = 60°	14.136	1.4658	0.7292	3.0038	1.3041	0.8712

In the higher rotor-harmonics ranges, each interval centres on a multiple of third rotor-harmonic (e.g., $6f_{rotor}$ and $9f_{rotor}$), again accompanied by wave-related sidebands. Both Fig. 23 and Table B.3 indicate that amplitudes decrease with increasing harmonic order. For rotor power and thrust, the amplitude at $6f_{rotor}$ generally lie between those at $2f_{wave}$ and $3f_{wave}$, while the amplitude at $9f_{rotor}$ is approximately equal to that of the $3f_{wave}$. In summary, the aerodynamic response shows limited variation. Although oblique waves affect rotor inflow via platform motion, the wind speed which maintained at the rated value remains the dominant factor influencing turbine performance.

References

Ai, C., Ma, Y., Zhang, J., Gao, Y., Liu, Y., Bu, S., 2025. A numerical study on motion responses of OC-4 DeepCwind floating wind turbine equipped with two different mooring configurations in combined wind and wave environments. Ocean Eng. 334, 121661. https://doi.org/10.1016/j.oceaneng.2025.121661.

Ananthan, S., Capone, L., Henry de Frahan, M., Hu, J.J., Melvin, J., Overfelt, J.R., Sharma, A., Sitaraman, J., Swirydowicz, K., Thomas, S., Vijayakumar, G., Williams, A.B., Yellapantula, S., Sprague, M., 2019. Nalu-Wind and OpenFAST: a high-fidelity modeling and simulation environment for wind energy. Sandia National Lab. (SNL-NM), Albuquerque, NM, United States; Sandia National Lab. SNL-CA), Livermore, CA, United States. https://doi.org/10.2172/1762093.

Bachant, P., Goude, A., Wosnik, M., 2016. Actuator line modeling of vertical-axis turbines. arXiv preprint arXiv:1605.01449. https://doi.org/10.48550/arXiv.1605.01449.

Bagbanci, H., Karmakar, D., Guedes Soares, C., 2012. Review of offshore floating wind turbines concepts. In: Soares, C.G., Garbatov, Y., Sutulo, S., Santos, T.A. (Eds.), Maritime Engineering and Technology. Taylor & Francis Group, London, pp. 553–562. https://www.taylorfrancis.com/chapters/edit/10.1201/b12726-80.

Berdugo-Parada, I., Servan-Camas, B., Garcia-Espinosa, J., 2024. Numerical framework for the coupled analysis of floating offshore multi-wind turbines. J. Mar. Sci. Eng. 12 (1), 85. https://doi.org/10.3390/jmse12010085.

Branlard, E., Jonkman, J., Platt, A., Thedin, R., Martínez-Tossas, L.A., Kretschmer, M., 2024. Development and verification of an improved wake-added turbulence model in FAST.Farm. J. Phys., Conf. Ser. 2767, 092036. https://doi.org/10.1088/1742-6596/2767/9/092036.

Cai, Y., Li, X., Zhao, H., Shi, W., Wang, Z., 2025. Developing a multi-region coupled analysis method for floating offshore wind turbine based on OpenFOAM. Renew. Energy 238, 122026. https://doi.org/10.1016/j.renene.2024.122026.

Campaña-Alonso, G., Martín-San-Román, R., Méndez-López, B., Benito-Cia, P., Azcona-Armendáriz, J., 2023. OF2: coupling OpenFAST and OpenFOAM for high-fidelity aero-hydro-servo-elastic FOWT simulations. Wind Energy Sci. 8 (10), 1597–1611. https://doi.org/10.5194/wes-8-1597-2023.

Cao, H., Wan, D., 2014. Development of multidirectional nonlinear numerical wave tank by Naoe-FOAM-SJTU solver. Int. J. Ocean Syst. Eng. 4 (1), 49–56. https://doi.org/10.5574/IJOSE.2014.4.1.049.

Chen, H., Hall, M., 2022. CFD simulation of floating body motion with mooring dynamics: coupling MoorDyn with OpenFOAM. Appl. Ocean Res. 124, 103210. https://doi.org/10.1016/j.apor.2022.103210.

Chen, P., Chen, J., Hu, Z., 2020. Review of experimental-numerical methodologies and challenges for floating offshore wind turbines. J. Mar. Sci. Appl. 19 (3), 339–361. https://doi.org/10.1007/s11804-020-00165-z.

Chen, X., Wang, T., Cai, C., Liu, J., Gao, X., Guo, N., Li, Q., 2025. A review of experiment methods, simulation approaches and wake characteristics of floating offshore wind turbines. J. Mar. Sci. Eng. 13 (2), 208. https://doi.org/10.3390/jmse13020208.

Cheng, P., Huang, Y., Wan, D., 2019. A numerical model for fully coupled aero-hydrodynamic analysis of floating offshore wind turbine. Ocean Eng. 173, 183–196. https://doi.org/10.1016/j.oceaneng.2018.12.021.

Choi, Y.-M., Kim, Y.J., Bouscasse, B., Seng, S., Gentaz, L., Ferrant, P., 2020. Performance of different techniques of generation and absorption of free-surface waves in computational fluid dynamics. Ocean Eng. 214, 107575. https://doi.org/10.1016/j.oceaneng.2020.107575.

Churchfield, M., Lee, S., Moriarty, P., 2012. Overview of the Simulator for Offshore Wind Farm Application (SOWFA). National Renewable Energy Lab., Golden, CO, United States. https://www.nrel.gov/wind/nwtc/sowfa.

Claus, R., López, M., 2022. Key issues in the design of floating photovoltaic structures for the marine environment. Renew. Sustain. Energy Rev. 164, 112502. https://doi.org/10.1016/j.rser.2022.112502.

Coulling, A.J., Goupee, A.J., Robertson, A.N., Jonkman, J.M., Dagher, H.J., 2013. Validation of a FAST semi-submersible floating wind turbine numerical model with DeepCwind test data. J. Renew. Sustain. Energy 5, 023116. https://doi.org/10.1063/1.4796197.

Deng, Y., Zhu, C., Zhang, S.Y., Yang, Y., Zhang, B., 2025. A novel coupling framework for integrating turbine and substructure dynamics of floating offshore wind turbines. Ocean Eng. 340, 122307. https://doi.org/10.1016/j.oceaneng.2025.122307.

Ding, W., Lin, G., Sun, H., Zhao, X., Ai, C., Liu, B., 2024. Effects of a multi-segment mooring system using buoy and clump weights on motions of the OC-4 DeepCwind wind turbine system under wind and waves. Ocean Eng. 296, 117018. https://doi.org/10.1016/j.oceaneng.2024.117018.

Esteban, M.D., Diez, J.J., López, J.S., Negro, V., 2011. Why offshore wind energy? Renew. Energy 36 (2), 444–450. https://doi.org/10.1016/j.renene.2010.07.009.

Fu, Z., Li, Y., Gong, J., Zhang, D., Li, A., 2021. Effect of sailing directions on the coupled motion and stability of trimaran in waves. Ocean Eng. 240, 109955. https://doi.org/10.1016/j.oceaneng.2021.109955.

Giri Ajay, A., Simao Ferreira, C., 2024. A numerical investigation of wake recovery for an H- and X-shaped vertical-axis wind turbine with wake control strategies. Phys. Fluids 36, 127161. https://doi.org/10.1063/5.0244810.

GWEC (Global Wind Energy Council), 2025. Global Wind Report. Brussels, Belgium.

Haider, R., Shi, W., Lin, Z., Cai, Y., Zhao, H., Li, X., 2024. Coupled analysis of floating offshore wind turbines with new mooring systems by CFD method. Ocean Eng. 312, 119054. https://doi.org/10.1016/j.oceaneng.2024.119054.

Hirt, C.W., Nichols, B.D., 1981. Volume of fluid (VOF) method for the dynamics of free boundaries. J. Comput. Phys. 39 (1), 201–225. https://doi.org/10.1016/0021-9991(81)90145-5.

Holthuijsen, L.H., 2010. Waves in Oceanic and Coastal Waters. Cambridge university press.

Hu, Z.Z., Greaves, D., Raby, A., 2016. Numerical wave tank study of extreme waves and wave-structure interaction using OpenFoam®. Ocean Eng. 126, 329–342. https://doi.org/10.1016/j.oceaneng.2016.09.017.

Huang, H., Liu, Q., Yue, M., Miao, W., Wang, P., Li, C., 2023. Fully coupled aero-hydrodynamic analysis of a biomimetic fractal semi-submersible floating offshore wind turbine under wind-wave excitation conditions. Renew. Energy 203, 280–300. https://doi.org/10.1016/j.renene.2022.12.060.

Huang, Y., Wan, D., 2020. Numerical analysis of aeroelastic responses of wind turbine under uniform inflow. Proceedings of the ASME 2020 39th International Conference on Ocean, Offshore and Arctic Engineering (OMAE2020). https://doi.org/10.1115/OMAE2020-18084. Virtual, Online, pp. V009T09A041.

Huang, Y., Yang, X., Zhao, W., Wan, D., 2024. Aeroelastic analysis of wind turbine under diverse inflow conditions. Ocean Eng. 307, 118235. https://doi.org/10.1016/j.oceaneng.2024.118235.

Jacobsen, N.G., 2017. waves2Foam Manual.

Jonkman, J., Butterfield, S., Musial, W., Scott, G., 2009. Definition of a 5-MW Reference Wind Turbine for Offshore System Development. National Renewable Energy Lab., Golden, United States https://doi.org/10.2172/1155123.

Jonkman, J.M., Buhl Jr., M.L., 2025. FAST User's Guide - Updated August 2005. National Renewable Energy Lab., Golden, CO, United States https://doi.org/10.2172/15020796.

Kim, Y.J., Charlou, M., Bouscasse, B., Leroy, V., Aliyar, S., Bonnefoy, F., Kim, K.-H., Choi, Y.-M., 2025. High fidelity simulations of a floating offshore wind turbine in irregular waves by coupling OpenFOAM and OpenFAST. Renew. Energy 243, 122486. https://doi.org/10.1016/j.renene.2025.122486.

Kurnia, R., Ducrozet, G., 2023. NEMOH: open-source boundary element solver for computation of first- and second-order hydrodynamic loads in the frequency domain. Comput. Phys. Commun. 292, 108885. https://doi.org/10.1016/j.cpc.2023.108885.

Li, P., Cheng, P., Wan, D., Xiao, Q., 2015. Numerical simulations of wake flows of floating offshore wind turbines by unsteady actuator line model. Proceedings of the 9th International Workshop on Ship and Marine Hydrodynamics, pp. 26–28. Glasgow, UK.

Li, Q., Wang, J., Yan, S., Gong, J., Ma, Q., 2018. A zonal hybrid approach coupling FNPT with OpenFOAM for modelling wave-structure interactions with action of current. Ocean Syst. Eng. 8 (4), 381–407. https://doi.org/10.12989/ose.2018.8.4.381.

Li, X., Zhu, C., Fan, Z., Chen, X., Tan, J., 2020. Effects of the yaw error and the wind-wave misalignment on the dynamic characteristics of the floating offshore wind turbine. Ocean Eng. 199, 106960. https://doi.org/10.1016/j.oceaneng.2020.106960.

Liao, X., Chen, X., Gui, H., Du, M., 2021. CFD prediction of ship seakeeping and slamming behaviors of a trimaran in oblique regular waves. J. Mar. Sci. Eng. 9 (10), 1151. https://doi.org/10.3390/jmse9101151.

Liu, Y., 2019. HAMS: a frequency-domain preprocessor for wave-structure interactions—theory, development, and application. J. Mar. Sci. Eng. 7 (3), 81. https://doi.org/10.3390/jmse7030081.

Liu, Y., Peng, Y., Wan, D., 2015. Numerical investigation on interaction between a semi-submersible platform and its mooring system. ASME 2015 34th International Conference on Ocean, Offshore and Arctic Engineering (OMAE2015). https://doi.org/10.1115/OMAE2015-41294. St. John's, Newfoundland, Canada, pp. V007T06A071.

Liu, Y., Xiao, Q., 2019. Development of a fully coupled aero-hydro-mooring-elastic tool for floating offshore wind turbines. J. Hydrodyn. 31 (1), 21–33. https://doi.org/10.1007/s42241-019-0012-6.

Liu, Y., Xiao, Q., Incecik, A., Peyrard, C., Wan, D., 2017. Establishing a fully coupled CFD analysis tool for floating offshore wind turbines. Renew. Energy 112, 280–301. https://doi.org/10.1016/j.renene.2017.04.052.

Lyu, G., Zhang, H., Li, J., 2019. Effects of incident wind/wave directions on dynamic response of a SPAR-type floating offshore wind turbine system. Acta Mech. Sin. 35 (5), 954–963. https://doi.org/10.1007/s10409-019-00884-9.

Micallef, D., Rezaeiha, A., 2021. Floating offshore wind turbine aerodynamics: trends and future challenges. Renew. Sustain. Energy Rev. 152, 111696. https://doi.org/10.1016/j.rser.2021.111696.

Muhammad, N., He, X., Jing, H., Zhao, Y., Ullah, Z., Zeng, S., 2025. Impact of wind-wave misalignment-induced motions on the power production of floating offshore wind turbine fowt. In: Yang, J., Fu, J., Liu, A., Ng, C.-T. (Eds.), Proceedings of the First International Conference on Engineering Structures. Springer Nature Singapore, Singapore, pp. 985–1000. https://doi.org/10.1007/978-981-96-4698-2_94.

Nam, B.W., Hwang, S.-C., Ha, Y.-J., Kim, K.-H., Hong, S.Y., Kim, H.J., Kim, J.W., Huang, Z.J., 2019. CFD modeling practice for sidewall greenwater problem of a FPSO in irregular waves. Proceedings of the 29th (2019) International Ocean and Polar Engineering Conference. ISOPE), Honolulu, Hawaii, USA, pp. 2912–2917. In: https://onepetro.org/ISOPEIOPEC/proceedings/ISOPE19/ISOPE19/ISOPE-I-19-079/20864.

NREL (National Renewable Energy Lab, 2025. OpenFAST documentation release v4.1.2. https://openfast.readthedocs.io/en/dev/index.html.

NREL Forum, 2025. AeroDyn output. https://forums.nrel.gov/t/aerodyn-outputs/392/. (Accessed 27 October 2025).

Otter, A., Murphy, J., Pakrashi, V., Robertson, A., Desmond, C., 2022. A review of modelling techniques for floating offshore wind turbines. Wind Energy 25 (5), 831–857. https://doi.org/10.1002/we.2701.

Pericàs, P.F., 2022. CFD Simulation of a Floating Wind Turbine with Openfoam: an FSI Approach Based on the Actuator Line and Relaxation Zone Methods (master's Thesis). Delft University of Technology Delft, The Netherlands. https://tudelft.on.worldcat.org/oclc/1358880270.

Ramachandran, R.C., Desmond, C., Judge, F., Serraris, J.J., Murphy, J., 2022. Floating wind turbines: marine operations challenges and opportunities. Wind Energy Sci. 7 (2), 903–924. https://doi.org/10.5194/wes-7-903-2022.

Robertson, A., Jonkman, J., Masciola, M., Song, H., Goupee, A., Coulling, A., Luan, C., 2014. Definition of the Semisubmersible Floating System for Phase II of OC4. National Renewable Energy Lab., Golden, CO, United States https://doi.org/10.2172/1155123.

Roddier, D., Cermelli, C., Aubault, A., Weinstein, A., 2010. WindFloat: a floating foundation for offshore wind turbines. J. Renew. Sustain. Energy 2 (3), 033104. https://doi.org/10.1063/1.3435339.

Shaler, K., Jonkman, J., Doubrawa Moreira, P., Hamilton, N., 2019. Fast.Farm Response to Varying Wind Inflow Techniques. California. AIAA Scitech 2019 Forum, San Diego, California, United States. https://doi.org/10.2514/6.2019-2086.

Shim, S., 2009. Coupled Dynamic Analysis of Floating Offshore Wind Farms (master's Thesis). Texas A&M University. https://hdl.handle.net/1969.1/ETD-TAMU-2564.

Sørensen, J.N., Shen, W.Z., 2002. Numerical modeling of wind turbine wakes. J. Fluid Eng. 124 (2), 393–399. https://doi.org/10.1115/1.1471361.

Tran, T.T., Kim, D.-H., 2016a. A CFD study into the influence of unsteady aerodynamic interference on wind turbine surge motion. Renew. Energy 90, 204–228. https://doi.org/10.1016/j.renene.2015.12.013.

Tran, T.T., Kim, D.-H., 2016b. Fully coupled aero-hydrodynamic analysis of a semi-submersible FOWT using a dynamic fluid body interaction approach. Renew. Energy 92, 244–261. https://doi.org/10.1016/j.renene.2016.02.021.

Vollmer, L., Steinfeld, G., Heinemann, D., Kühn, M., 2016. Estimating the wake deflection downstream of a wind turbine in different atmospheric stabilities: an LES study. Wind Energ. Sci. 1 (2), 129–141. https://doi.org/10.5194/wes-1-129-2016.

Wang, J., Zhao, W., Wan, D., 2019. Development of naoe-FOAM-SJTU solver based on OpenFOAM for marine hydrodynamics. J. Hydrodyn. 31 (1), 1–20. https://doi.org/10.1007/s42241-019-0020-6.

Wang, S., Moan, T., Jiang, Z., 2022. Influence of variability and uncertainty of wind and waves on fatigue damage of a floating wind turbine drivetrain. Renew. Energy 181, 870–897. https://doi.org/10.1016/j.renene.2021.09.090.

Wei, D., Zhao, W., Wan, D., Xiao, Q., 2021. A new method for simulating multiple wind turbine wakes under yawed conditions. Ocean Eng. 239, 109832. https://doi.org/10.1016/j.oceaneng.2021.109832.

Xu, S., Xue, Y., Zhao, W., Wan, D., 2022. A review of high-fidelity computational fluid dynamics for floating offshore wind turbines. J. Mar. Sci. Eng. 10 (10), 1357. https://doi.org/10.3390/jmse10101357.

Xu, S., Yang, X., Zhao, W., Wan, D., 2024. Numerical analysis of aero-hydrodynamic wake flows of a floating offshore wind turbine subjected to atmospheric turbulence inflows. Ocean Eng. 300, 117498. https://doi.org/10.1016/j.oceaneng.2024.117498.

Xu, S., Zhuang, T., Zhao, W., Wan, D., 2023. Numerical investigation of aerodynamic responses and wake characteristics of a floating offshore wind turbine under atmospheric boundary layer inflows. Ocean Eng. 279, 114527. https://doi.org/10.1016/j.oceaneng.2023.114527.

Xue, Y., Wang, J., Zhao, W., Wan, D., 2025. Numerical analysis of effects of wind-wave-current interactions on the performance of floating offshore wind turbine. Proceedings of the 35th (2025) International Ocean and Polar Engineering Conference. ISOPE, Seoul/Goyang, Korea, pp. 279–287. In: https://onepetro.org/ISOPEIOPEC/proceedings/ISOPE25/ISOPE25/ISOPE-I-25-043/713093.

Xue, Y., Yang, X., Wan, D., 2024. Numerical investigation of aero and hydrodynamic response of floating offshore wind turbine under Ochi-Hubble Bi-Modal wave spectrum. Proceedings of the 34th (2024) International Ocean and Polar Engineering Conference. ISOPE, Rhodes, Greece, pp. 834–842. In: https://onepetro.org/ISOPEIOPEC/proceedings/ISOPE24/ISOPE24/ISOPE-I-24-120/546510.

Yang, Y., Bashir, M., Michailides, C., Li, C., Wang, J., 2020. Development and application of an aero-hydro-servo-elastic coupling framework for analysis of floating offshore wind turbines. Renew. Energy 161, 606–625. https://doi.org/10.1016/j.renene.2020.07.134.

Yu, Z., Ma, Q., Zheng, X., Liao, K., Sun, H., Khayyer, A., 2023. A hybrid numerical model for simulating aero-elastic-hydro-mooring-wake dynamic responses of floating offshore wind turbine. Ocean Eng. 268, 113050. https://doi.org/10.1016/j.oceaneng.2022.113050.

Zhang, W., Calderon-Sanchez, J., Duque, D., Souto-Iglesias, A., 2024. Computational Fluid Dynamics (CFD) applications in Floating Offshore Wind Turbine (FOWT)

dynamics: a review. Appl. Ocean Res. 150, 104075. https://doi.org/10.1016/j.apor.2024.104075.
Zhou, Y., Xiao, Q., Liu, Y., Incecik, A., Peyrard, C., Li, S., Pan, G., 2019. Numerical modelling of dynamic responses of a floating offshore wind turbine subject to focused waves. Energies 12 (18), 3482. https://doi.org/10.3390/en12183482.
Zhou, Y., Xiao, Q., Liu, Y., Incecik, A., Peyrard, C., Wan, D., Pan, G., Li, S., 2022. Exploring inflow wind condition on floating offshore wind turbine aerodynamic characterisation and platform motion prediction using blade resolved CFD simulation. Renew. Energy 182, 1060–1079. https://doi.org/10.1016/j.renene.2021.11.010.